Earth-Science Reviews 245 (2023) 104563

Contents lists available at ScienceDirect

Earth-Science Reviews

journal homepage: www.elsevier.com/locate/earscirev

Etna 2011–2022: Discoveries from a decade of activity at the volcano

Marisa Giuffrida [a], Massimiliano Cardone [a], Francesco Zuccarello [b], Marco Viccaro [a,b,*]

[a] Dipartimento di Scienze Biologiche Geologiche e Ambientali, Università di Catania, Corso Italia 57, I-95129 Catania, Italy
[b] Istituto Nazionale di Geofisica e Vulcanologia - Sezione di Catania, Osservatorio Etneo, Piazza Roma 2, I-95125 Catania, Italy

ARTICLE INFO

Keywords:
Etna
Paroxysmal eruptions
Plumbing system dynamics
Diffusion chronometry
Olivine crystals

ABSTRACT

We present here a comprehensive petrological investigation of products emitted during the December 2020 – February 2022 paroxysmal sequence occurred at the South East Crater of Mt. Etna, interpreting results within the framework of the post-2011 activity at the volcano in order to provide a realistic illustration of the evolution of the volcano plumbing system throughout the last decade. We have combined thermodynamic modeling on whole rock with micro-analytical data on volcanic crystals and glasses to investigate the physical and chemical conditions of magmas involved and the kinetics of magma movements among the different levels of the plumbing system. Whole rock major element compositions indicate changes in storage conditions and transfer dynamics starting from eruptions at the Voragine on December 2015. These data also highlight that the 2020–22 eruptions have been fed by the most mafic magma with respect to all the eruptions of the last decade. Chemical heterogeneities of olivine crystals confirm the activation, during the first months of 2021, of the most mafic magmatic environments characterizing the feeding system of Mt. Etna if compared to the whole last decade. This mafic magma has permeated all the plumbing system of Mt. Etna throughout the 2021, driving periods of more frequent eruptions depending on the possibility to have efficient drainage at shallow levels, with patterns similar to those observed during the 2011–13 sequence. Fe-Mg diffusion chronometry applied to zoned olivine from the first phase of the 2020–22 sequence (December 13, 2020 – April 1, 2021) allows us to detect fast migration of the mafic magma from the deepest level of the plumbing system upward to intermediate and shallow levels, with times comparable to those leading to the astonishing paroxysmal eruptions of 2015–16 at Voragine. Connections among the magmatic environments during the second phase of the paroxysmal sequence (May 19, 2021 – February 21, 2022) chiefly involve the intermediate and shallow levels of the volcano feeding system, with timescales of magma transfer slower than those registered during the first phase. This study highlights that replenishment by volatile-rich magmas from the deepest levels of the plumbing system is a recurrent trend over the last decade at Mt. Etna and that the effusive vs. explosive activity at the surface is related with the injected volumes and the magma ability to degas during the ascent.

1. Introduction

During its eruptive history, Mt. Etna has given birth to a wide spectrum of eruptions from both the summit craters and the volcano flanks. While the eruptive behavior typically includes mild Strombolian eruptions and lava effusions, there has been a clear growth in the number of high-energy explosive eruptions at the volcano summit during the last four decades (Armienti et al., 1996; Corsaro and Pompilio, 2004; Clocchiatti et al., 2004; Corsaro and Miraglia, 2014; Behncke et al., 2014; Cannata et al., 2015; Corsaro et al., 2017; Edwards et al., 2018; Calvari et al., 2022). In particular, the last decade has seen a significant increase in eruption frequency together with the development of some of the most energetic paroxysmal sequences recorded at Mt. Etna in recent times. These include the three-year-long sequence of lava fountaining during 2011–13 (Giuffrida and Viccaro, 2017) and the very recent sequence of eruptions that took place between December 2020 and February 2022 at the South East Crater (hereafter SEC; Fig. 1; Calvari et al., 2022). These two sequences are separated by fairly long period of dominant effusive activity, such as in 2014 and 2017–2020 (De Beni et al., 2015, 2019; Cappello et al., 2019), which were interrupted only by the two short, but powerful paroxysmal series that occurred at Voragine (hereafter VOR; Fig. 1) during December 2015 and May 2016 (Corsaro et al., 2017; Cannata et al., 2018; Edwards et al., 2018).

* Corresponding author at: Dipartimento di Scienze Biologiche Geologiche e Ambientali, Università di Catania, Corso Italia 57, I-95129 Catania, Italy.
E-mail address: marco.viccaro@unict.it (M. Viccaro).

https://doi.org/10.1016/j.earscirev.2023.104563
Received 27 February 2023; Received in revised form 24 August 2023; Accepted 28 August 2023
Available online 9 September 2023

The latest paroxysmal sequence began on December 13, 2020 after nearly two years of continuous, though weak, explosive activity at the summit, chiefly at the VOR and SEC. Sixty-two episodes of powerful lava fountains took place in slightly more than one year, with the highest frequency of eruptions falling into two main periods, the first during February 16 – April 1, 2021 whereas the second during May 19 – July 14, 2021. The entire 2020–22 sequence was characterized by the rising of eruptive columns of up to ~13 km of height a.s.l. (Calvari et al., 2022) that were followed by abundant tephra fallout on the volcano slopes and ash dispersion up to hundreds of kilometers.

Frequent changes in the eruptive style and shifts in the location of volcanic activity in the summit area have occurred during the last decade. These observations have posed the need of detailing the ascent pathway of distinct magma batches through the complex plumbing system of the volcano, a network of variably connected sill-like storage zones and dykes, defining how the conditions of storage, transfer and interaction of magmas have changed over time. Accordingly, the analysis and correlation of compositionally-zoned crystals coming from subsequent eruptions has become a routine practice for tracking the evolution of Mt. Etna plumbing system dynamics over recent and past periods of activity. Petrological diffusion chronometry-based approaches that make use of the chemical information preserved in various mineral phases (e.g., plagioclase, olivine and pyroxene) have been successfully applied to investigate extended periods of volcanic activity, as for the 1607–2013 (Viccaro et al., 2016a), 1974–2014 (Ubide and Kamber, 2018), 1991–2008 (Kahl et al., 2015) and 2011–2013 (Giuffrida and Viccaro, 2017; Giuffrida et al., 2018), as well as individual eruptive episodes (Kahl et al., 2017; Magee et al., 2020). Following the end of the 2011–13 eruptive sequence, continuous association of petrological observations with geophysical monitoring signals has produced advanced models of the plumbing system architecture, strongly emphasizing the short-term variability in storage conditions and ascent dynamics of the last decade (Viccaro et al., 2016b, 2019; Cannata et al., 2018; Borzì et al., 2020; Giuffrida et al., 2021).

In this contribution, whole rock, crystal and glass chemistry of tephra from the 2020–22 paroxysmal sequence have been inspected in the framework of the previous post-2011 volcanic activity with the aim of documenting the plumbing system evolution throughout the last decade. We provide new constraints on the thermodynamic properties of the modern Etnean plumbing system and on the kinetics of magmatic processes taking place beneath the volcano. A careful examination and comparison of the newly acquired dataset for the 2020–22 activity with the existing petrographic and geochemical data for volcanic products of the post-2011 activity (data provided by Viccaro et al., 2015, 2016a, 2019; Giuffrida and Viccaro, 2017; Pompilio et al., 2017; Cannata et al., 2018; Borzì et al., 2020; Giuffrida et al., 2021; Miraglia, 2021; Corsaro and Miraglia, 2022) has offered the chance to clearly evaluate changing modes and timescales of magma storage and transport at Mt. Etna and how they can impact the development of paroxysmal eruptions.

2. Volcanological background

2.1. An overview of Mt. Etna eruptive history

Mt. Etna is one of the most studied and best monitored volcanoes on Earth, being among the few that erupt nearly continuously from the summit craters. Yet, it can produce eruptions from vents and fissures on its flanks. Mt. Etna rises to the height of 3357 m on eastern Sicily (Southern Italy) at the suture zone between the African and European continental plates in an area of geodynamic complexities where the Apennine-Maghrebian Chain overlaps the undeformed margin of the African continental plate, and bounded eastwards by the subducting oceanic Ionian lithosphere (Fig. 1; Lentini, 1982).

Early volcanism in this area began about 500 ka ago with fissure-type eruptions emplacing tholeiitic basalts in a submarine environment (Tanguy, 1978; Gillot et al., 1994). The eruption of subaerial tholeiites date back to 330 ka (Gillot et al., 1994), whose remnants still outcrop on

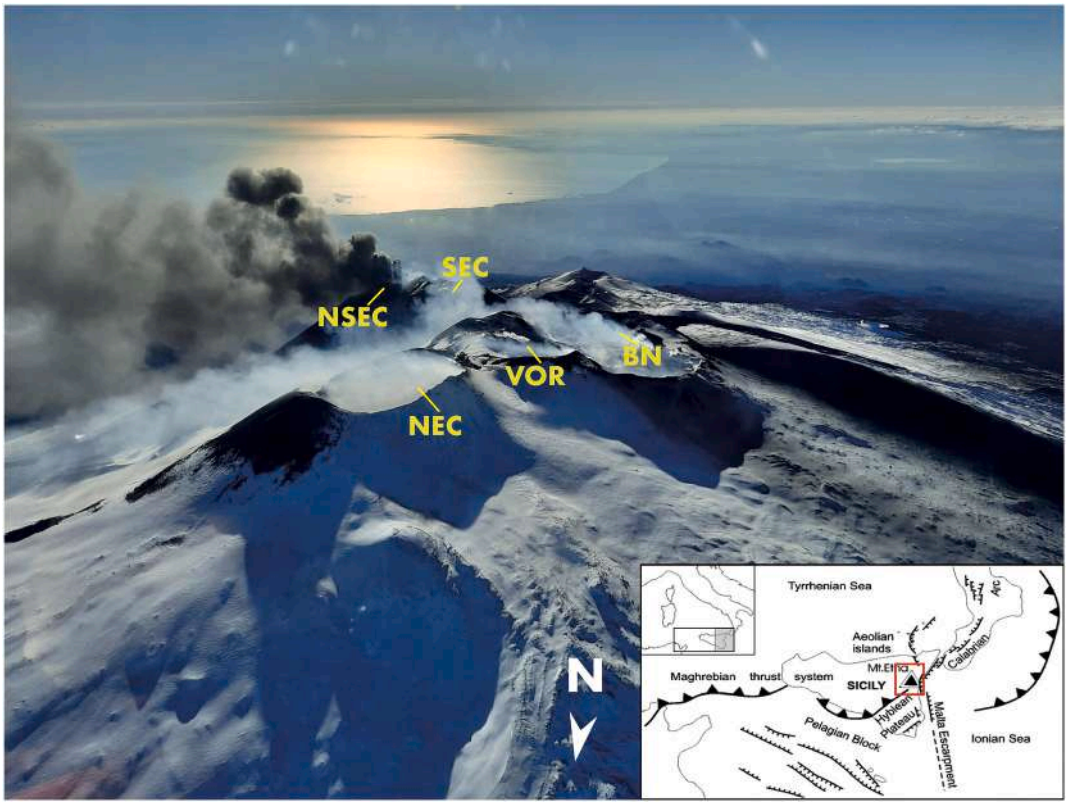

Fig. 1. View of the Mt. Etna summit area with location of the five craters at the date of January 7, 2021. NSEC: New South East Crater; SEC: South East Crater; BN: Bocca Nuova; VOR: Voragine; NEC: North East Crater. The inset shows the regional setting of Mt. Etna within the geodynamic framework of Southern Italy.

the SW slopes of the volcano. Starting from about 220 ka ago, erupted lavas changed composition from subalkaline toward Na-alkaline, while the major eruptive axes, initially concentrated on the Ionian coast (Fig. 1), migrated westwards, gradually aligning themselves on a central conduit during the last 130 ka (Tanguy et al., 1997; Branca et al., 2008). The last 130 ka mark the transition from fissure to central vent activity that occurred with cycles of Strombolian to Plinian eruptions and led to the construction of a series of central-conduit edifices mostly localized in the Valle del Bove depression. The central activity definitively stabilized ~57 ka ago. Large stratovolcanoes were built at a later stage of this phase, as a consequence of persistent volcanic activity, both effusive and highly explosive, localized in the area of the present-day Etna edifice.

The recent volcanic history of Mt. Etna (15 ka to present) began with the growth of the Mongibello stratovolcano, whose products form most of the present edifice (Branca and Del Carlo, 2004). In the last 15 ka, volcanic activity has been highly variegated, changing from purely effusive to violent explosive through summit and flank eruptions. Last few centuries were dominated by effusive eruptions and Strombolian ejections with production of hawaiites and, to a lesser extent, mugearites (Branca and Del Carlo, 2004). Increasing eruption frequency and explosivity have been documented since 1971, concurrently with compositional changes of volcanic products that became K-trachybasalts (Tanguy and Clocchiatti, 1984; Armienti et al., 1996; Tonarini et al., 1995; Tanguy et al., 1997; Viccaro and Cristofolini, 2008; Viccaro et al., 2011; Viccaro and Zuccarello, 2017). While experiencing fluctuation in eruption frequency and style, Mt. Etna has been particularly active in the last 30 years (Harris et al., 2011; Bonaccorso and Calvari, 2013; Bisson et al., 2021). Over this period, we have witnessed noteworthy eruptions, some of the fissure type that produced large lava flow fields, as in 1991–93 (Armienti et al., 1994), 2004–05 (Fornaciai et al., 2021) and in 2008–09 (Bonaccorso et al., 2011) and scoria cones, as in 2001 and 2002–03 (Andronico et al., 2005). Since 1989, there was also a clear growth in the number of paroxysmal eruptions from the summit craters. These brief, powerful events were able to generate km-height eruptive columns, abundant tephra fallouts and ash dispersion up to hundreds of km far from craters. Paroxysmal episodes of Mt. Etna have usually occurred in short-term sequence of multiple events lasting weeks to years. Recent sequences remarkable for the eruption energy took place at the SEC in 1998–99 (23 events in 6 months; La Delfa et al., 2001), 2000 (64 events in 6 months; Andronico and Corsaro, 2011) and 2007 (7 events in 7 months; Andronico et al., 2008). Since then, other 113 paroxysmal episodes have occurred.

2.2. The post-2011 volcanic activity

Since January 2011, a new vent placed just to southeast of the SEC, named New South East Crater (NSEC), became the main site of a three-year-long sequence of 44 lava fountains (Behncke et al., 2014; Viccaro et al., 2015; Giuffrida and Viccaro, 2017). This sequence ended in December 2013, nonetheless the NSEC remained the leading actor of Mt. Etna summit activity of the following years, at least until the first half of 2019, while the other four craters [i.e., Bocca Nuova (BN), North East Crater (NEC), VOR and SEC; Fig. 1] have been intermittently active (Fig. 2a). The activity at NSEC was dominated by Strombolian explosions of variable intensity and lava effusions during 2014–15, and became increasingly more effusive in the following years, in particular

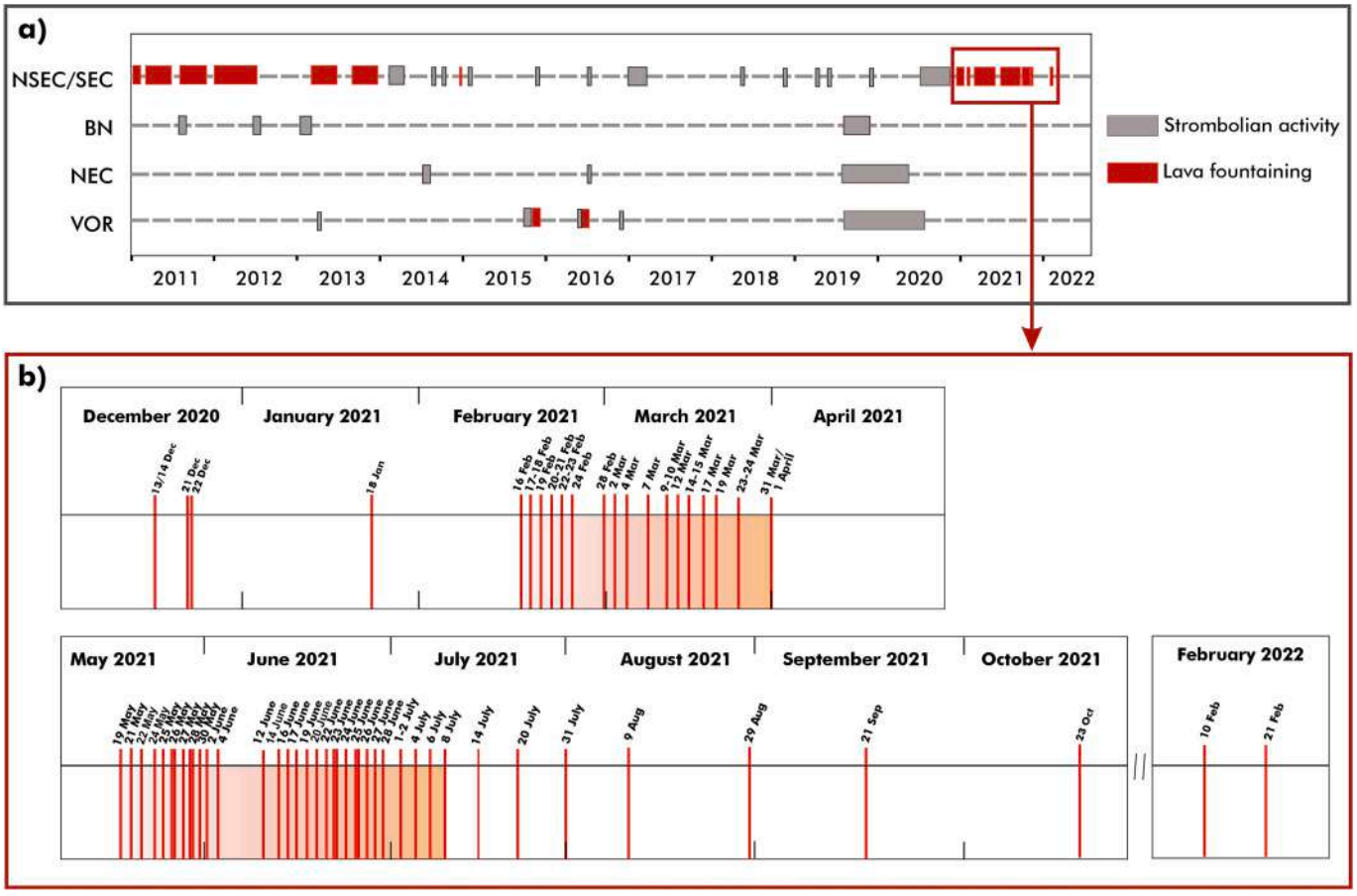

Fig. 2. a) Schematic representation of the eruptive activity at Mt. Etna from January 2011 to February 2022; this panel shows the main eruptive periods at NSEC/SEC, BN, NEC and VOR, distinguishing both the styles of eruptive activity and the erupting vents. The rectangular area in red corresponds to the blow-up of the panel b). b) Sequence of paroxysmal eruptions occurred from December 2020 to February 2022; red-shaded colored areas refer to periods with the highest eruption frequency. (For interpretation of the references to colour in this figure legend, the reader is referred to the web version of this article.)

after the two short, but powerful series of paroxysmal eruptions that occurred at VOR in December 2015 (4 events; Aloisi et al., 2017; Corsaro et al., 2017) and May 2016 (3 episodes; Cannata et al., 2018; Edwards et al., 2018). The end of the 2016 paroxysmal activity at VOR marked not only the beginning of a new dominantly effusive eruptive phase involving both the summit (e.g., in February–April 2017; De Beni et al., 2019; Currenti and Bonaccorso, 2019; Viccaro et al., 2019) and the volcano flanks (e.g., in December 2018; Borzì et al., 2020; Calvari et al., 2020; Paonita et al., 2021), but also a clear decrease of the eruptive frequency with the occurrence of relatively long periods of quiescence (Fig. 2a). The 2019–20 was a period of intensification of the volcanic activity at all the summit craters, which culminated with some main effusive phases from fissures opened at the base of the NSEC in May and July 2019. The last months of 2019 have also seen the reawakening of VOR after years of volcanic activity dominated by eruptions at the NSEC (Fig. 2a; Giuffrida et al., 2021; Bruno et al., 2022). VOR gave birth to persistent Strombolian activity of variable intensity that lasted for eight months, causing the spreading of lava flows within the nearby BN until the end of April 2020. Strombolian explosions and ash emissions continued at all summit craters throughout the 2020, with a progressive re-activation of the SEC-NSEC complex (Fig. 2a). Between the summer of 2020 and the autumn of the same year, due to numerous internal collapses, all the fissures present in the saddle between the SEC and the NSEC unified forming one single large cone, i.e. the SEC from that moment on.

2.3. The December 2020–February 2022 paroxysmal sequence

Between December 13, 2020 and February 21, 2022, Mt. Etna has produced sixty-two paroxysmal explosive eruptions from the SEC (Fig. 2b; Table 1). All paroxysms have evolved in a similar way, starting with Strombolian activity that progressively intensify to lava fountains followed by the formation of eruptive columns rising several kilometers above the craters, and accompanied by short-lasting rheomorphic lava flows formed by agglutination of tephra fallout (Costa et al., 2023). The first eruptive episode of the sequence occurred on the late evening of December 13, 2020 after a gradual increase of the Strombolian explosive activity at the summit craters producing incandescent lava jets at ~20:35 UTC that were visible from the INGV monitoring cameras EMOT (Calvari et al., 2022). At ~21:30 UTC, jets of lava from the crater rim were almost continuous, evolving into a sustained fountaining activity in just 30 min. The fountaining phase lasted only 48 min. During this time, three pyroclastic density currents (PDCs) formed at 22:15, 22:16 and 22:30 UTC as a consequence of the collapse of the accumulated pyroclasts on the SW flank of the SEC, followed by the output of two small lava flows spreading southwestward and eastward for a few hundred meters until midnight (Calvari et al., 2022). Explosive activity at the vent stopped at 10:48 UTC. Two further, yet shorter fountain pulses were observed at 23:58 and at 01:02 UTC on December 14, 2020, respectively. In all cases, the height of lava fountaining was quite low, reaching a maximum of about 550 m above the crater rim during the first pulse, and then lowering to a maximum height of 300–400 m during the second and the third pulses.

While displaying similar evolutionary phases, the 61 paroxysmal eruptions that followed that of December 13–14, 2020 differ from each other in magnitude and intensity, as well as in duration (Calvari and Nunnari, 2022). In the timespan between December 2020 and February 2022, the estimated erupted volumes for individual paroxysms varied from 0.2 to 5 $\times$ 10^6 m^3, whereas discharge rates are in the range of 59–232 m^3/s (Calvari and Nunnari, 2022; Ganci et al., 2023). After the fountain phases of December 13–14, 2020, two more episodes occurred in December 2020, and one in January 2021 (Fig. 2b; Table 1). A relentless succession of 17 episodes from the SEC started on February 16 and concluded on April 1 (Fig. 2b; Table 1). This phase includes some of the most energetic events of the entire 2020–22 sequence, such as the episodes of February 28, during which lava fountaining lasted 63 min, forming in a short time a vertically rising eruptive column up to ~9000 m above the summit (Calvari et al., 2022). This event and many others during February–April 2021 were characterized by high volume of erupted pyroclastic materials, up to maximum volumes of ~4 $\times$ 10^6 m^3 (e.g., in the night between March 31 and April 1, 2021; Calvari and Nunnari, 2022). Hereafter, we will refer to the sequence of eruptions between December 13, 2020 and April 1, 2021, as first eruptive phase.

After a pause of about 1 month and half since the paroxysmal eruption of March 31–April 1, 2021, a second eruptive phase begun on May 19 and continued up to February 21, 2022, producing 41 new lava fountaining episodes from SEC (Fig. 2b; Table 1). Within this second phase, the frequency of eruptions was particularly high in the period May–July 2021, with 31 events until July 8 (Fig. 2b; Table 1). After July 8, the frequency gradually decreases through the second half of July (3 events separated by 6 to 11 days of pause between subsequent episodes) and during the next months of August (2 events on August 9 and 29), September (1 event on September 21) and October 2021 (1 event on October 23) with pauses of 20 to 31 days from one episode to the other (Fig. 2b; Table 1). The last two paroxysmal eruptions of the sequence occurred on February 10 and 21, respectively (Fig. 2b; Table 1), only preceded by a small effusive event occurred on the western flank of the Valle del Bove on December 13–14, 2022.

3. Petrological features of volcanic products emitted between 2011 and 2022

3.1. Petrography and mineral chemistry

Many studies over the last decade have provided extensive petrochemical information for both lavas and tephra associated to the main phases of the explosive and effusive activity recorded at Mt. Etna since 2011 (e.g., Viccaro et al., 2014, 2015, 2016a, 2016b, 2019; Mollo et al., 2015, 2022; Giacomoni et al., 2018; Corsaro et al., 2017; Giuffrida and Viccaro, 2017; Pompilio et al., 2017; Cannata et al., 2018; Edwards et al., 2018; Ubide and Kamber, 2018; Borzì et al., 2020; Giuffrida et al., 2021; Miraglia, 2021; Corsaro and Miraglia, 2022).

The suite of volcanic products erupted in the period 2011–22 shares rather similar petrographic and geochemical features with some minor differences (Fig. 3). Both lavas and tephra are notably vesiculated (from ~30% up to >80% of vesicles by volume according to X-ray microtomography measurements and observations by scanning electron microscope; Pompilio et al., 2017; Lanzafame et al., 2018; Edwards et al., 2021). All products are porphyritic, with an anhydrous mineral assemblage consisting of plagioclase [$An_{44–91}$; An = 100 $\times$ Ca/(Ca + Na + K) mol%], olivine [$Fo_{65–89}$; Fo = 100 $\times$ Mg/(Mg + Fe + Mn) mol%], clinopyroxene [Mg# 70–82; $DiHd_{0.71–0.83}$; Mg# = 100 $\times$ Mg/(Mg + Fe^{2+}) mol%] and opaque oxides (titaniferous magnetite, in general). The phase assemblage is identical in all the products and includes phenocrysts, micro-phenocrysts and microlites that have been here discriminated on the basis of the longest axis > 0.3 mm, 0.3–0.1 mm, and < 0.1 mm, respectively (Armienti et al., 1984). The phenocryst and microphenocryst content is 15–30 vol% in tephra and 25–35 vol% in lava rocks. Phenocrysts and micro-phenocrysts set in a groundmass of varying crystallinity that mostly contains microlites of acicular plagioclase. Air-quenched scoria clasts from lava fountains have a vitrophyric groundmass showing low microlite content (<15 vol%), suggesting that the late-stage crystallization was hampered by the rapid quenching of magma. The lava flow samples display moderately to highly crystalline groundmass (30–40 vol% of microlites) with scarce residual glass. It is not unusual the coexistence of rock portions displaying different groundmass textures, often visible at the thin-section scale. For instance, sharp transitions from vitrophyric to hyalopilitic groundmass texture are features frequently observed in the scoriae erupted during 2011–13 and 2015–16 (Giuffrida and Viccaro, 2017; Pompilio et al., 2017; Cannata et al., 2018).

Table 1
Chronology of the 62 paroxysmal eruptions occurred during the period December 2020 – February 2022. The time of starting and intensification of the Strombolian activity derives from the volcanic activity reports published by the INGV – Etnean Observatory available at www.ct.ingv.it, while the time of starting and ending of the lava fountaining phase, height and volume of erupted tephra are from Calvari and Nunnari (2022).

No. of event	Date (dd.mm.yyyy)	Start of Strombolian activity (UTC)	Intensification of Strombolian activity (UTC)	Start of lava fountain (UTC)	End of lava fountain (UTC)	Total fountaining duration (min)	Lava fountain height (m)	Tephra volume $10^6 \times m^3$
1	13–14/12/2020	n.a.	13/12/2020 19.20	13/12/2020 22.00	14/12/2020 1.40	220	280	0.06
2	21/12/2020	n.a.	n.a.	21/12/2020 9.11	21/12/2020 9.59	48	1390	0.13
3	22/12/2020	n.a.	22/12/2020 2.50	22/12/2020 3.05	22/12/2020 5.13	128	516	0.84
4	18/01/2021	n.a.	18/01/2021 19.15	18/01/2021 19.38	18/01/2021 21.03	85	901	0.37
5	16/02/2021	n.a.	n.a.	16/02/2021 16.11	16/02/2021 17.02	51	1330	0.44
6	17–18/02/2021	17/02/2021 22.30	n.a.	17/02/2021 22.32	18/02/2021 0.51	139	1105	1.04
7	19/02/2021	n.a.	n.a.	19/02/2021 8.16	19/02/2021 10.06	110	1096	0.84
8	20–21/02/2021	20/02/2021 17.30	20/02/2021 20.23	20/02/2021 21.32	21/02/2021 1.15	223	738	1.33
9	22–23/02/2021	22/02/2021 20.50	n.a.	22/02/2021 21.17	23/02/2021 0.03	166	1727	1.43
10	24/02/2021	24/02/2021 16.12	24/02/2021 17.18	24/02/2021 18.56	24/02/2021 21.41	165	1384	1.61
11	28/02/2021	28/02/2021 7.10	n.a.	28/02/2021 7.31	28/02/2021 8.34	63	2502	0.75
12	02/03/2021	02/03/2021 10.45	n.a.	02/03/2021 11.23	02/03/2021 14.50	207	333	0.15
13	04/03/2021	04/03/2021 0.20	04/03/2021 1.00	04/03/2021 7.11	04/03/2021 9.32	141	1450	1.34
14	07/03/2021	07/03/2021 1.00	07/03/2021 3.30	07/03/2021 4.10	07/03/2021 7.01	171	552	0.35
15	09–10/03/2021	09/03/2021 18.30	n.a.	09/03/2021 23.55	10/03/2021 2.46	171	765	0.03
16	12/03/2021	12/03/2021 2.40	n.a.	12/03/2021 7.35	12/03/2021 9.45	130	1579	1.61
17	14–15/03/2021	14/03/2021 20.20	n.a.	14/03/2021 23.12	15/03/2021 1.42	150	1121	0.66
18	17/03/2021	17/03/2021 0.50	n.a.	17/03/2021 1.30	17/03/2021 4.57	207	502	0.42
19	19/03/2021	17/03/2021 6.17	n.a.	19/03/2021 8.18	19/03/2021 10.13	115	679	0.58
20	23–24/03/2021	23/03/2021 19.05	n.a.	23/03/2021 21.33	24/03/2021 8.19	646	390	0.28
21	31/03–01/04/2021	31/03/2021 17.50	n.a.	31/03/2021 19.30	01/04/2021 8.53	803	588	3.7
22	19/05/2021	19/05/2021 0.20	n.a.	19/05/2021 0.50	19/05/2021 4.25	215	469	1.41
23	21/05/2021	20/05/2021 23.34	n.a.	21/05/2021 0.50	21/05/2021 2.44	114	748	0.97
24	22/05/2021	22/05/2021 8.14	n.a.	22/05/2021 20.27	22/05/2021 22.08	101	899	0.95
25	24/05/2021	24/05/2021 19.20	n.a.	24/05/2021 20.25	24/05/2021 21.49	84	1265	0.91
26	25/05/2021	25/05/2021 16.20	25/05/2021 16.45	25/05/2021 18.20	25/05/2021 18.53	33	349	0.21
27	26/05/2021	26/05/2021 1.19	26/05/2021 1.45	26/05/2021 1.55*	26/05/2021 3.47*	112	n.a.	n.a.
28	26/05/2021	26/05/2021 8.06	n.a.	26/05/2021 10.20	26/05/2021 11.10	50	660	0.39
29	27/05/2021	n.a.	n.a.	27/05/2021 12.50	27/05/2021 12.59	9	839	0.13
30	28/05/2021	28/05/2021 6.00	n.a.	28/05/2021 6.30	28/05/2021 7.27	57	496	0.4
31	28/05/2021	28/05/2021 19.35	n.a.	28/05/2021 19.48	28/05/2021 20.50	62	376	0.04
32	30/05/2021	30/05/2021 3.45	n.a.	30/05/2021 4.20	30/05/2021 5.44	84	589	0.46
33	02/06/2021	02/06/2021 7.44	02/06/2021 8.00	02/06/2021 8.30	02/06/2021 10.46	136	576	0.64
34	04/06/2021	02/06/2021 18.50	04/06/2021 13.30	04/06/2021 16.12	04/06/2021 17.40	88	1672	1.09
35	12/06/2021	08/06/2021 23.10	12/06/2021 11.30	12/06/2021 20.00	12/06/2021 21.46	106	582	0.72
36	14/06/2021	n.a.	n.a.	14/06/2021 21.15	14/06/2021 22.21	66	726	0.47
37	16/06/2021	n.a.	16/06/2021 11.32	16/06/2021 11.37	16/06/2021 12.38	61	1338	0.33
38	17/06/2021	16/06/2021 15.20	17/06/2021 20.20	17/06/2021 22.40	17/06/2021 23.55	75	665	0.49
39	19/06/2021	19/06/2021 18.15	19/06/2021 18.40	19/06/2021 18.47	19/06/2021 19.35	48	727	0.38
40	20/06/2021	20/06/2021 21.00	20/06/2021 21.53	20/06/2021 22.40	20/06/2021 23.44	64	1265	0.72
41	22/06/2021	22/06/2021 2.15	22/06/2021 2.30	22/06/2021 2.30	22/06/2021 3.45	75	955	0.68
42	23/06/2021	23/06/2021 0.30	n.a.	23/06/2021 2.44	23/06/2021 3.19	35	993	0.3
43	23/06/2021	23/06/2021 17.17	23/06/2021 17.45	23/06/2021 18.00	23/06/2021 19.12	72	1412	0.57
44	24/06/2021	24/06/2021 9.05	n.a.	24/06/2021 9.45	24/06/2021 10.26	41	1528	0.55

(*continued on next page*)

Table 1 (*continued*)

No. of event	Date (dd.mm.yyyy)	Start of Strombolian activity (UTC)	Intensification of Strombolian activity (UTC)	Start of lava fountain (UTC)	End of lava fountain (UTC)	Total fountaining duration (min)	Lava fountain height (m)	Tephra volume $10^6 \times m^3$
45	25/06/2021	24/06/2021 23.17	24/06/2021 23.50	25/06/2021 0.38	25/06/2021 1.48	70	1265	0.42
46	25/06/2021	25/06/2021 17.39	25/06/2021 18.05	25/06/2021 18.40	25/06/2021 19.20	40	1065	0.35
47	26/06/2021	26/06/2021 14.30	n.a.	26/06/2021 16.00	26/06/2021 16.38	38	1250	0.39
48	27/06/2021	27/06/2021 7.12	n.a.	27/06/2021 8.53	27/06/2021 9.43	50	704	0.47
49	28/06/2021	28/06/2021 14.01	n.a.	28/06/2021 14.25	28/06/2021 15.30	65	2136	0.71
50	01–02/07/2021	01/07/2021 22.40	n.a.	01/07/2021 22.50	02/07/2021 00.27	97	1339	0.76
51	04/07/2021	04/07/2021 14.56	n.a.	04/07/2021 15.15	04/07/2021 16.50	95	1228	0.83
52	06/07/2021	06/07/2021 21.30	n.a.	06/07/2021 22.16	06/07/2021 23.44	88	2809	1.12
53	08/07/2021	08/07/2021 19.00	08/07/2021 19.55	08/07/2021 20.35	08/07/2021 22.12	97	1858	1.07
54	14/07/2021	14/07/2021 9.05	n.a.	14/07/2021 10.45	14/07/2021 12.30	105	2177	1.23
55	20/07/2021	19/07/2021 22.00	n.a.	20/07/2021 5.10	20/07/2021 8.11	181	2271	1.73
56	31/07/2021	31/07/2021 17.15	31/07/21 17.50	31/07/2021 19.44	31/07/2021 23.37	233	2205	2.45
57	09/08/2021	08/08/2021 22.30	09/08/21 0.40	09/08/2021 2.07	09/08/2021 4.11	124	1808	1.39
58	29/08/2021	29/08/2021 15.25	n.a.	29/08/2021 16.24	29/08/2021 17.55	91	2460	1.09
59	21/09/2021	21/09/2021 6.55	n.a.	21/09/2021 7.21	21/09/2021 8.35	74	1640	0.9
60	23/10/2021	n.a.	n.a.	23/10/2021 8.20	23/10/2021 10.17	117	2414	1.66
61	10/02/2022	n.a.	n.a.	10/02/2022 18.40	10/02/2022 21.56	196	5060	2.28
62	21/02/2022	n.a.	n.a.	21/02/2022 11.11	21/02/2022 12.50	99	2231	1.33

* Data from published reports by the INGV – Etnean Observatory available at www.ct.ingv.it

The relative abundances of the mineral phases described above vary little in the deposits of different eruptive periods. Plagioclase forms the 40–60 vol% of the total crystal content, ranking as the dominant mineral phase in all volcanic products erupted between 2011 and 2022. Clinopyroxene constitutes the 20–35 vol% of crystals. Olivine is always in percentage <15 vol%. Titaniferous magnetite composes 5–7 vol% of the crystals content and occurs mainly in the groundmass or as inclusions in olivine and clinopyroxene. While the abundances between mineral phases remain somewhat constant, the spectrum of crystal compositions and textural characteristics is large through the decade.

Typically, plagioclase is the most destabilized phase, displaying both equilibrium and disequilibrium textures resulting in a variety of chemical zoning patterns from core to rim in accordance to what has been observed for past eruptions at Mt. Etna (Viccaro et al., 2010, 2014, 2016a; Nicotra and Viccaro, 2012a, 2012b). Giuffrida and Viccaro (2017) provided a comprehensive overview of the range of plagioclase textures and compositions in products of the 2011–13 period of activity. The characteristics of plagioclase observed by Giuffrida and Viccaro (2017) are recurrent over time and have been broadly documented in volcanic products of the whole decade (Mollo et al., 2015; Viccaro et al., 2016a, 2016b, 2019; Giuffrida et al., 2018; Cannata et al., 2018; Borzì et al., 2020; Giuffrida et al., 2021). The same features continue to be present in volcanic products of the 2021–22 paroxysmal sequence. Plagioclase phenocrysts display pervasive resorption, particularly at the core, and major dissolution surfaces between discrete zones having distinct anorthite concentrations. The chemical contrast between adjacent zones in correspondence of dissolution surfaces is typically high (ΔAn_{30-45}), with compositional jumps that can cover the range andesine-anorthite. Dissolution and resorption are poorly noticeable in micro-phenocrysts and absent in microlites, both manifest as clear, fine-scale oscillatory zoned crystals in response of near-equilibrium crystallization. Clear oscillatory zoned plagioclases that show just small anorthite variations (ΔAn_{5-10}) along the entire core-to-rim profile usually coexist with unzoned olivine crystals.

Clinopyroxene occurs as augite and diopside ($Wo_{43-49}En_{35-52}Fs_{12-21}$). The Mg# varies from 70 to 89, but typically, individual crystals are quite homogeneous in major elements from core to rim. The measured Mg# values along core-to-rim crystal transects show small fluctuations in the order of $\Delta Mg\# \sim 2$. Phenocrysts and micro-phenocrysts consist of a combination of distinctive textural features that includes sector and concentric zoning characterized by the alternance of compositionally-distinct zones (Ubide and Kamber, 2018; Mollo et al., 2022), as well as resorption textures at the crystal rim. The latter is a feature typical of large (>500 μm) augitic clinopyroxene found in scoria clasts from the sequences of lava fountains (Viccaro et al., 2014; Giuffrida and Viccaro, 2017). Except for the crystals with evidence of resorption at the rim, the habit of large clinopyroxene phenocrysts is prismatic and euhedral with defined planar edges. Phenocrysts frequently enclose sub-rounded micro-phenocrysts and microlites of opaque oxides.

Olivine occurs as microlites, micro-phenocrysts and phenocrysts with size up to 1.5 mm. The largest olivine crystals are usually affected by disequilibrium that manifests as embayments at the rim (Zuccarello et al., 2022). These crystals coexist with destabilized augitic clinopyroxene. When comparing the spectrum of olivine composition between tephra and lavas emitted in the post-2011 period, the olivine from fallout materials turned out to be overall more forsteritic (Fo_{68-89}) than olivine from lava rocks (Fo_{65-84}). Cores are chemically more homogeneous than rims. Rims characterize, instead, for the variety of zoning patterns, from simple normal or reverse to highly complex zoning. The compositional variability of olivine crystals erupted in the present decade has been the focus of many studies attempting to extract key information on the Mt. Etna plumbing system architecture and dynamics (Kahl et al., 2011, 2013, 2015; Mollo et al., 2015; Viccaro et al., 2015, 2016a, 2019; Giuffrida and Viccaro, 2017; Cannata et al., 2018; Borzì et al., 2020; Giuffrida et al., 2021). The existing petrological studies report an increase in the average olivine Fo core composition since the

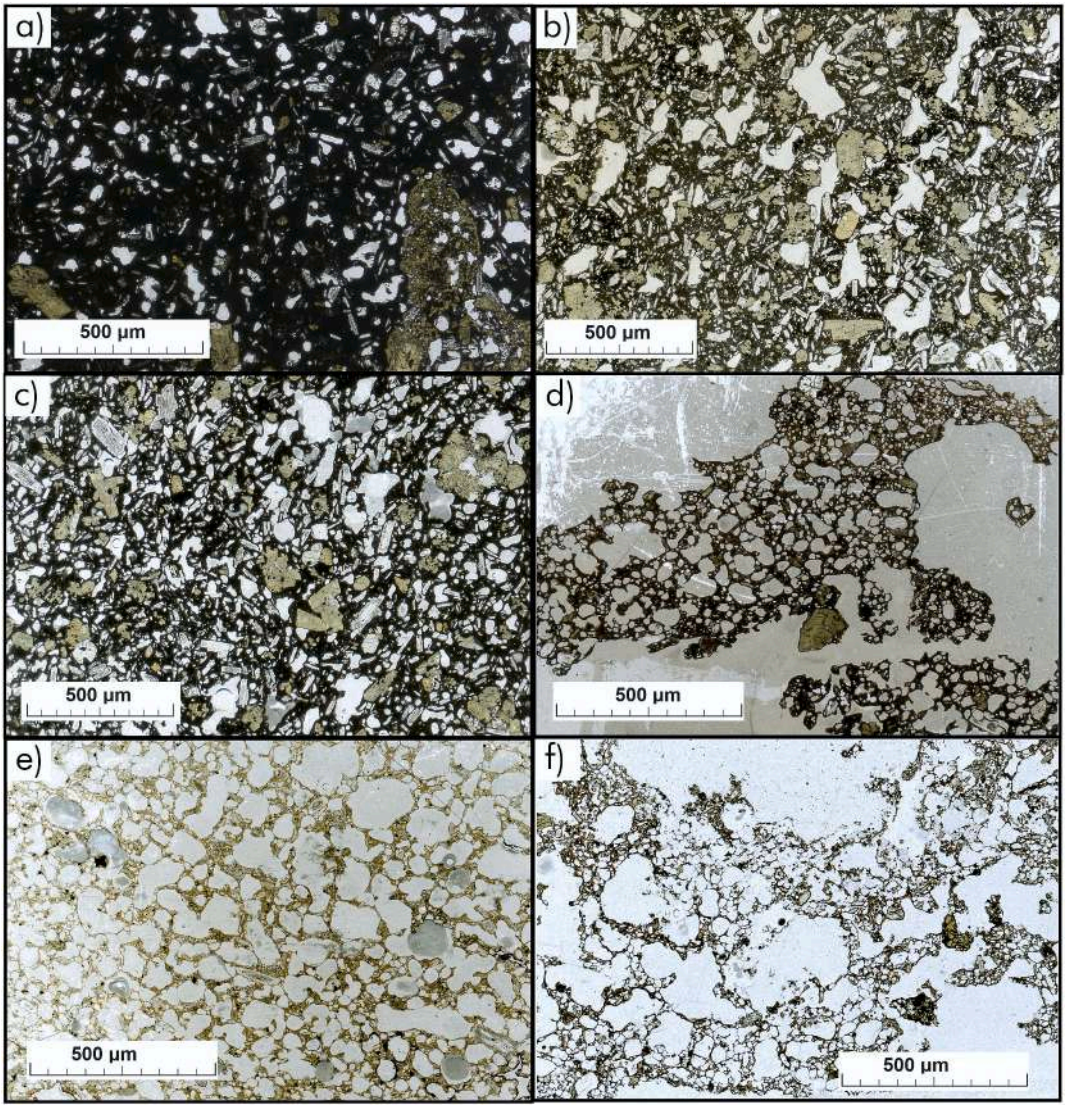

Fig. 3. Textural characteristics of representative volcanic products erupted at Mt. Etna during the 2011–2022 period: a) lava of the September 28, 2011 paroxysmal episode at the SEC; b) lava of the 2017 eruption at the SEC; c) lava of the December 24–27, 2018 flank eruption in Valle del Bove; d) tephra of the December 3, 2015 paroxysmal eruption at VOR; e) tephra from the January 24, 2020 explosive activity at VOR; f) tephra from the February 17–18, 2021 paroxysmal eruption at SEC.

activity of 2011–13 that has seen the extrusion of Mg-rich (Fo_{84}) olivine, not detected since the '80s (Kahl et al., 2015). In the following years, the volcanic activity produced even more mafic (Fo_{84} to Fo_{88}) olivine compositions that manifested with particular high frequency in the recent 2020–22 products. As this study is mostly focused on the compositional variability of olivine erupted in the present decade, we provide a quantitative comparison between olivine crystals from different eruptive phases coupled with detailed characterizations of the chemical zoning in Section 5.1 of this study.

Opaque oxides are titaniferous magnetites that are frequently enclosed in clinopyroxene and olivine phenocrysts, suggesting early nucleation and growth. Titaniferous magnetite micro-phenocrysts preferentially develop on pre-existing clinopyroxenes, whereas titaniferous magnetite phenocrysts grow as isolated crystals or form aggregate with clinopyroxene. Titaniferous magnetite microlite are abundant in the groundmass.

3.2. Geochemical characteristics of whole rocks and glasses

Tephra and lava rocks erupted between 2011 and 2022 are K-trachybasalts just as all the volcanic rocks erupted in recent time since 1971, when a clear shift toward the K-alkaline suite coupled with an enrichment in some LILE's (Rb, Cs) and depletion in HFSE's (Th) has occurred (Condomines et al., 1995; Tanguy et al., 1997; Viccaro and Cristofolini, 2008).

A huge amount of chemical analyses on whole rock and volcanic glass are available for the eruptions of the last decade (Viccaro et al., 2015, 2019; Pompilio et al., 2017; Miraglia, 2021; Corsaro and Miraglia, 2022). The new whole rock data collected for the 2020–22 paroxysmal sequence have been integrated with published analyses for the period 2011–20 that were carried out in the same laboratories (Viccaro et al., 2015, 2019). These data are shown in Supplementary Material 1 and have been plotted on Harker diagrams using SiO_2 as differentiation index (Fig. 4). The total silica content varies from 49.3 to 46.3 wt% on anhydrous basis. The volcanic rocks emitted in 2020–22 display a more mafic nature compared to the other products erupted during the last decade. The most primitive whole rock compositions refer to the paroxysmal episode of February 28, 2021 (SiO_2 46.3–46.6 wt%; MgO 6.6–6.9 wt%), which shows Mg# ~55 and CaO/Al_2O_3 ~ 0.75. The emission of very mafic products was not confined to this eruption; in fact, some other samples within the 2020–22 volcanic suite have MgO >6.5 wt% and $CaO/Al_2O_3 > 0.7$, such as those related to the eruptions of

February 16 and 22, 2021, and some lava fountains of the period June–July and September 2021 (Supplementary Material 1).

When considering the overall WR variability of all investigated products within the decade, Al_2O_3, alkalis and P_2O_5 correlate positively with SiO_2, while TiO_2, MgO, FeO and CaO correlate negatively (Fig. 4; Supplementary Material 1). However, a bimodal distribution is evident for all oxides, except for MgO. Volcanic rock compositions between December 2015 and January 2020 follow a common evolutionary pattern, where compositions of the 2020–22 and 2017 products constitute the mafic and evolved end-members, respectively. Whole rock compositions for the 2011–13 products differ from those of the 2015–22 series for lower CaO and higher FeO_{tot}, TiO_2 and alkalis, drawing a different trend of differentiation and indicating a different clinopyroxene plus plagioclase control on the liquid line of descent (Supplementary Material 1). These features overall support the idea that magmas feeding the paroxysmal activity of 2011–13 have a chemical signature somewhat different to that of the post-2015 magmas.

Major element compositions of volcanic glasses have been measured in tephra from 48 lava fountains in the period December 2020–October 2021 (Supplementary Material 1). In Fig. 5, these glass compositions are plotted in a CaO/Al_2O_3 vs. FeO_{tot}/MgO diagram. The glass compositional fields for the eruptions of 2015 at VOR (Pompilio et al., 2017) and 2013 at NSEC (Miraglia, 2021) were also plotted for comparison. The compositional fields defined by these three paroxysmal sequences partially overlap, albeit the 2015 glasses cover the largest chemical range (Fig. 5a). The glass chemistry of 2020–22 has lower FeO_{tot}/MgO

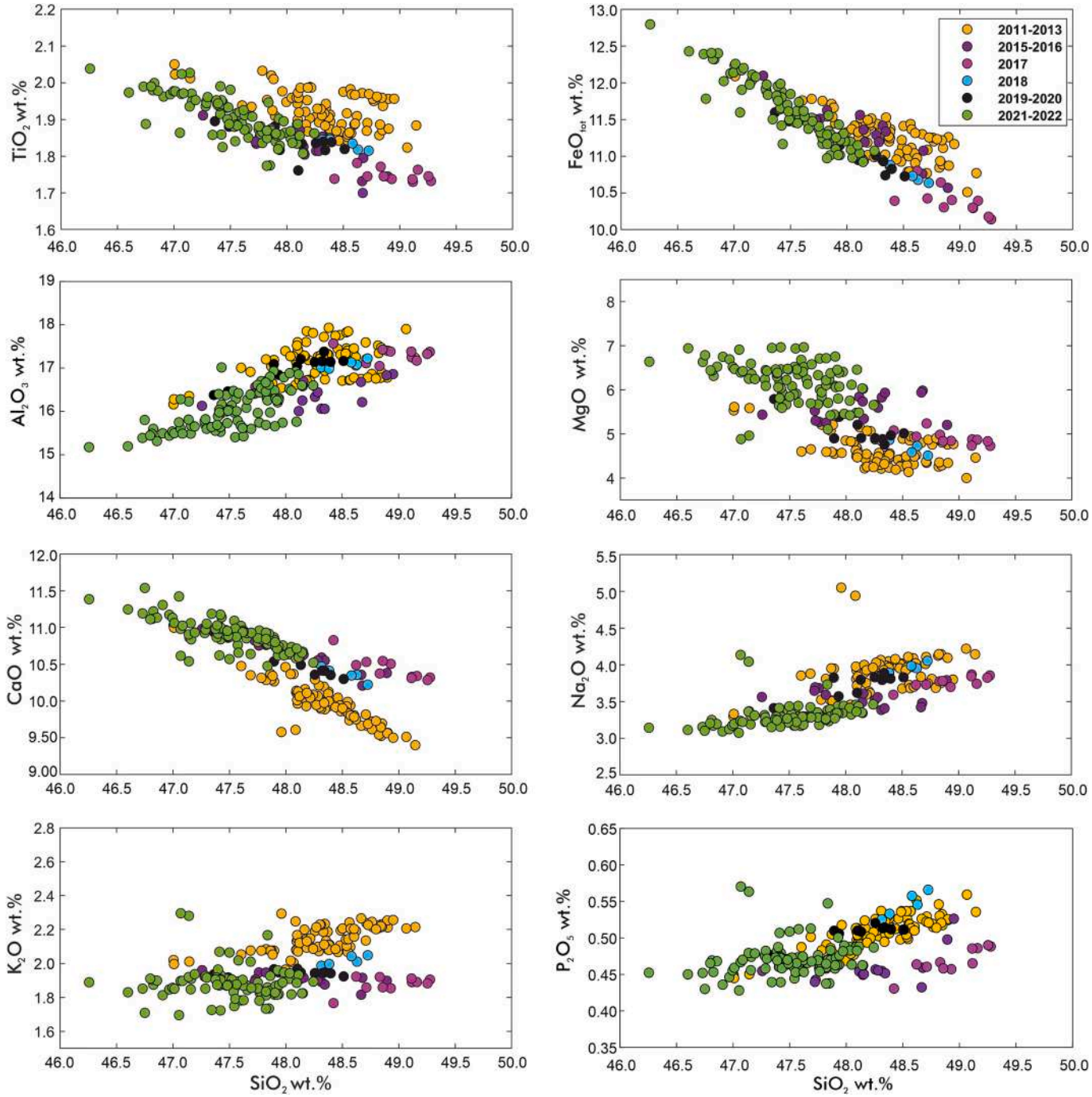

Fig. 4. Variation of major oxides for volcanic rocks erupted during the 2011–22 period (data sources available in the Supplementary Material 1).

ratio, in the range 1.8–3.1, than the 2013 and 2015 glasses, but comparable CaO/Al_2O_3. In Fig. 5b-c, the glass analyses of samples are plotted on the CaO/Al_2O_3 vs. FeO_{tot}/MgO diagram in two temporal series, one from December 2020 to May 2021 (Fig. 5b) that includes compositions of the first eruptive phase, and one from May 2021 to February 2022 (Fig. 5c) that incorporates compositions of the second phase of the paroxysmal sequence. Because volcanic glass can be assumed to be representative of the pre-eruptive magma composition, the plots can be used to qualitatively evaluate if the liquid becomes more or less primitive through time (cf. Corsaro and Miraglia, 2022).

The main compositional trend defined by the volcanic glasses highlights a compositional change toward mafic compositions from the early episodes of December 2020 to February 2021. Then, compositions became progressively more evolved from February to May 2021, following a trend of fractional crystallization (FC; Fig. 5b). The early eruptive events of the second phase of the 2020–22 series, which started on May 19, 2021, emitted rocks with compositions similar to those erupted at the end of the first phase (i.e., during the episode of March 31–April 1, 2021; cf. Corsaro and Miraglia, 2022; Supplementary Material 1). Again, a trend reversal in the evolution of the glass chemistry is observed for the following events, with compositions becoming progressively more mafic from May 2021 to February 2022 (Fig. 5c). Only the eruption of September 21 deviates from the main compositional trend that distinguish the second phase of the 2020–22 sequence, as this episode produced rocks with glass composition slightly more evolved than those of August, and compositionally more akin to those erupted during June–July 2021.

4. The 2011–20 plumbing system of Mt. Etna: Magmatic environments and thermodynamic constraints

Petrology of erupted products has resulted to be a key element to recognize depth of provenance and to track the ascent path of magma within the plumbing system of Mt. Etna. The knowledge on such a complex plumbing system has improved since regular monitoring of the volcano was established (Bonaccorso et al., 2004) and petrological data started to be integrated with geophysical measurements. In this regard, the integration of petrological data with seismic and infrasonic signals (Viccaro et al., 2016b; Cannata et al., 2018; Giuffrida et al., 2021) and ground deformation measurements (Viccaro et al., 2016b, 2019; Cannata et al., 2018; Borzì et al., 2020) has greatly contributed to unravel the connection between pre-eruptive magma dynamics and volcanic activity.

In previous studies, the compositional and zoning record of olivine crystals from some relevant summit and flank eruptions of the last decade was combined with Fe-Mg diffusion chronometry to reconstruct the history of magma migration throughout the plumbing system. A careful inspection of zoning profiles, from core to rim, gave access to the sequential growth of olivine under various physical-chemical conditions, allowing to track the magmatic environments a crystal passes through while moving to the surface. This approach proved to be effective in detailing the architecture of the Mt. Etna plumbing system, as well as in detecting changes in the kinetics of magma storage, ascent, and recharge over the past decade. The same approach is adopted here in an attempt to pursue the previous studies and interpret the sequence of volcanic events of 2020–22 in light of the present knowledge on Mt. Etna plumbing system architecture and dynamics and the observed variations in rock and crystal chemistry.

Following the systems analysis approach to compositionally zoned olivine of Kahl et al. (2011, 2013, 2015), Giuffrida and Viccaro (2017) studied the compositional and zoning record of 49 olivine crystals that were erupted between 2011 and 2013 at Mt. Etna. Correlating the zoning profiles of distinct olivine populations, Giuffrida and Viccaro (2017) tracked the pathway of magmas between distinct section of the plumbing system, providing new key information on the dynamics that took place from the deepest portions of the volcano edifice (≥20 km), in proximity to the crust-mantle boundary, to subsurface levels. These authors used thermodynamic calculations with the rhyolite-MELTS software (Ghiorso and Sack, 1995; Asimow and Ghiorso, 1998) to constrain the conditions of crystallization of the observed olivine populations, which showed nearly constant core compositions ranging from Fo_{70} to Fo_{84} resulting in roughly flat profiles, i.e., chemical plateaus. In accordance with the study of Kahl et al. (2015), the occurrence of these compositional plateaus in olivine crystals was interpreted as the consequence of crystal growth under constant thermodynamic conditions that define a certain magmatic environment. This is because to produce growth zones of constant forsterite content, the physical and chemical conditions of the hosting melt must have been kept constant for a certain period of time, otherwise variations in the compositional gradient and the development of normal or reverse zoning profiles would be expected, as observed due to cooling, fractionation or recharge (Kahl et al., 2015). Based on the systematic observation and distribution of distinct Fo plateaus for the 2011–13 period, Giuffrida and Viccaro (2017) have discriminated between multiple olivine populations, whose core composition realistically replicates the initial conditions of crystal formation. Specifically, the core composition of the erupted olivines

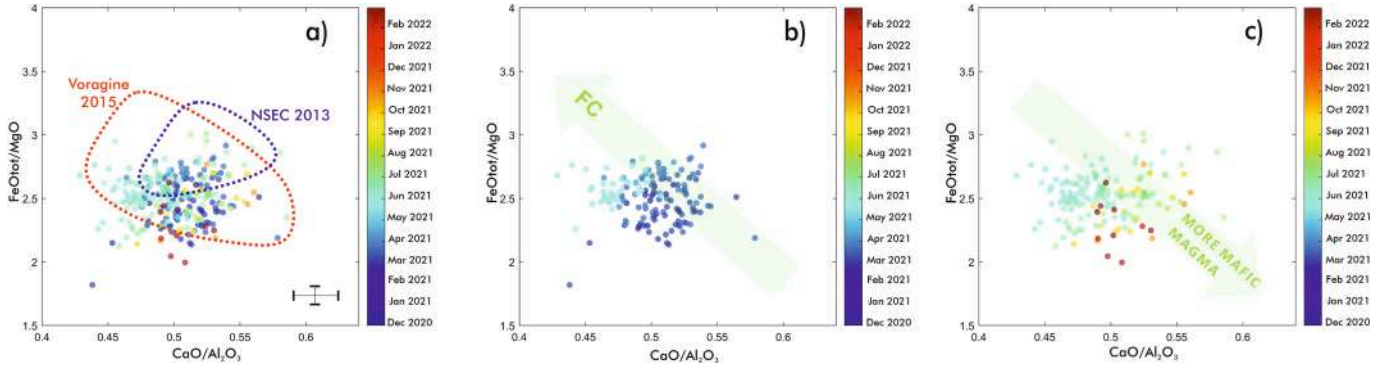

Fig. 5. a) CaO/Al_2O_3 vs. FeO_{tot}/MgO diagram for glasses in products erupted during the paroxysmal activity of December 2020–February 2022. The glass compositional fields of the 2015 eruptions at VOR (Pompilio et al., 2017) and at the NSEC in 2013 (Miraglia, 2021) are plotted for comparison; b) CaO/Al_2O_3 vs. FeO_{tot}/MgO in glasses of volcanic products erupted between December 2020 and May 2021. The green arrow indicates the expected fractional crystallization trend (FC) from the most mafic compositions of February 2021 to one of the most evolved of May 2021; c) CaO/Al_2O_3 vs. FeO_{tot}/MgO in glasses of volcanic products erupted between May 2021 and February 2022. The green arrow indicates compositions becoming more mafic from May 2021 to February 2022. The temporal variation of the erupted products is depicted by the colored bars. (For interpretation of the references to colour in this figure legend, the reader is referred to the web version of this article).

during 2011–13 suggested the existence of at least five main crystallization environments (M_i), which are distinguished by their own thermodynamic variables, i.e., pressure, temperature, composition and oxygen fugacity. The environments appear to be physically separated, though variably connected to each other. The deepest and most mafic recognized environment, labeled M_{00}, defines the crystallization condition of the Fo_{84} olivine at depth of ~18–20 km below the summit (T = 1210–1190 °C; P = 650–550 MPa; fO_2 1–1.9 × 10^{-7} bars). As the magma moves upwards, it can intercept the environments M_0 ($Fo_{80–82}$; T = 1156–1160 °C; P = 380–400 MPa; fO_2 = 3.5–3.0 × 10^{-9} bars), M_{1a} (Fo_{78}; T = 1126–1136 °C; P = 230–290 MPa; fO_2 = 1.4–1.0 × 10^{-9} bars), M_{1b} ($Fo_{75–76}$; T = 1104–1112 °C; P = 120–160 MPa; fO_2 = 5.9–4.7 × 10^{-10} bars) and M_2 ($Fo_{70–73}$; $T \leq 1088$ °C; $P \leq 30$ MPa; $fO_2 \leq$ 2.3 × 10^{-10} bars) following multiple independent routes of migration, while experiencing both crystal and fluid fractionation.

Since the work of Giuffrida and Viccaro (2017), the same set of thermodynamic variables have been routinely used to describe the crystallization environments of all olivine crystals erupted between 2014 and 2020, as the core populations observed during 2011–13 continued to be present in the volcanic products of the following years (Fig. 6). However, the total range in Fo concentration has expanded from 2014 onward, spanning from a minimum of Fo_{67} to a maximum of Fo_{89} at the crystal rim, suggesting the activation of a magmatic environment deeper and more mafic than M_{00}. It is worth to note that this set of thermodynamic variables was used even though the best-fit of the hypothetical liquid line of descent with the compositions of erupted products produced a minor shift since 2015, a feature that became markedly more emphasized for products erupted during the 2020–22 paroxysmal sequence. In this regard, we provide a new set of thermodynamic modeling able to reproduce the wide spectrum of crystallization conditions experienced by magmas over the period 2011–22 in section 5.2 of this review.

Viccaro et al. (2016b) provided the first evidence of such a primitive environment by analyzing the olivine assemblage of lava rocks erupted in 2014 at NEC. These authors documented the occurrence of one single olivine crystal having Fo_{86} core. Next, high forsteritic compositions (>Fo_{84}) were detected during the eruptive phases of VOR in 2015–16 (Cannata et al., 2018) and NSEC in 2018 (Fig. 6; Borzì et al., 2020). Cannata et al. (2018) reported the presence of olivine reverse zoning displaying increasing Fo content up to $Fo_{85–89}$ and surrounding chemically homogeneous $Fo_{80–82}$ cores, and attributed this feature to the injection of a primitive magma that rose up from very deep regions of the plumbing system (>650 MPa). Since then, a new magmatic environment, labeled M_x (Cannata et al., 2018) was introduced to reflect the conditions of crystallization of the olivine cores with composition >Fo_{85}. The observation of such mafic compositions at the core of olivine crystals was limited to just few crystals erupted on December 24–27, 2018 (Borzì et al., 2020), which showed maximum Fo concentration of 86 mol% as in 2014. Instead, they are completely missing in crystals from 2017 and 2019–2020, where olivine cores at $Fo_{80–82}$ form the most mafic core population (Viccaro et al., 2019; Giuffrida et al., 2021). Fig. 6 also shows the comparison of the compositional range of the olivine core populations erupted at Mt. Etna between 2011 and 2020 with those observed during the 2020–22 paroxysmal sequence (see Section 5.1 for details on the 2020–22 sequence).

Data from previous studies also stressed how olivines from different eruptive periods were characterized by different zoning patterns, which overall have put into evidence some differences in the storage and transfer dynamics of magmas that have fed these eruptions. Recharging phases by mafic magmas with the composition of M_x, M_{00} or M_0 are recurrent processes that have facilitated the transfer of magma to the surface by pressurizing the shallow and intermediate portions (≤ 290 MPa) of the plumbing system for the entire decade. However, the trigger of highly energetic paroxysmal eruptions was found to be related to the fast ascent of deep, undegassed magmas that directly migrate to very shallow crustal levels in short times (1–3 months), with little or no intermediate phases of storage and differentiation.

The post-2016 volcanic periods were dominated by effusive and weak-to-mild explosive activity and occurred in response of prolonged periods of deep mafic replenishment that pushed upwards more differentiated magmas residing in the intermediate reservoirs, triggering minor events of magma injection at shallow levels (Viccaro et al., 2019; Borzì et al., 2020; Giuffrida et al., 2021). This behavior was already inferred for past effusive eruptions at Mt. Etna (e.g., Di Grazia et al., 2009; Bonforte et al., 2017; Ubide and Kamber, 2018). Since the end of paroxysmal activity at VOR in May 2016, available data on olivine zoning supported the occurrence of repeated episodes of magma replenishment affecting the upper reservoirs mostly in correspondence

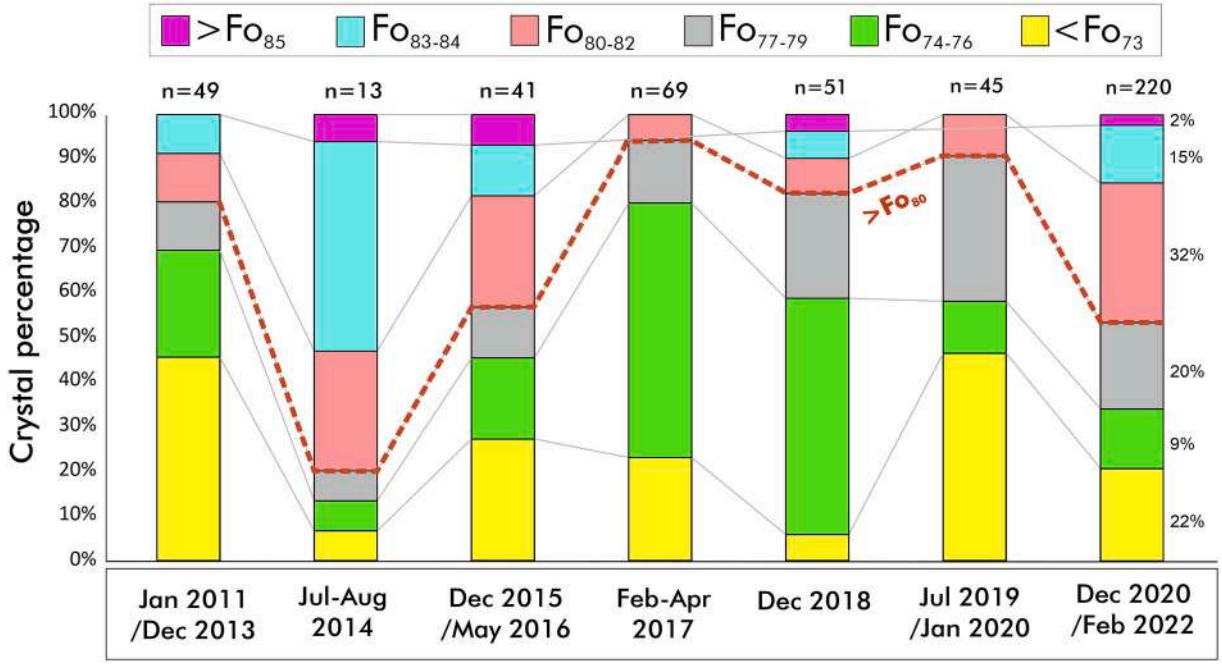

Fig. 6. Comparison of the distribution of olivine core compositions in different periods of volcanic activity at Mt. Etna from 2011 to 2022.

of the M_{1a} and M_{1b} environments. These findings agree with the geophysical evidence of a main zone of magma storage and differentiation extending between ~2 and 6 km b.s.l (i.e., within the pressure ranges of M_{1a} and M_{1b}; Bonaccorso et al., 2011; Patanè et al., 2013). Petrology confirmed that in the period between mid-2016 and the end of 2020 this section of the plumbing system was regularly refilled by injection of new mafic magmas that intermittently fed persistent eruptive activity at the summit craters, as in February–April 2017 at NSEC (Viccaro et al., 2019), in 2019–20 at NSEC-VOR (Giuffrida et al., 2021) and flank eruptions as in December 24–27, 2018 (Borzì et al., 2020).

5. Storage zones and recharging processes inferred from the chemical record of olivine from the 2020–22 eruptive cycle

5.1. Chemical zoning of olivine crystals from the 2020–22 paroxysmal eruptions

In accordance with existing petrographic descriptions of the recent Etnean products, there exists a large chemical variability in terms of core-to-rim composition in olivine of the 2020–22 eruptive cycle. Newly acquired data on 220 olivine crystals integrated in this study show the presence of olivine phenocrysts with normal, reverse or more complex zoning patterns and overall composition from Fo_{87} to Fo_{68} (Supplementary Material 2). A feature common to many phenocrysts is that Fe-Mg zoning profiles often contain core and/or rim compositional plateaus, i.e., olivine zones that are quite homogeneous in composition and show small Fo fluctuations on the order of 1–2 mol%. These homogeneous zones are variously connected one to the other by normal or reverse zoning patterns. Compositional plateaus typically characterize the inner cores of olivine, yet they also occur at the outer rims and/or at intermediate envelopes between the core and rim, with compositions embracing six main compositional ranges, i.e., $Fo_{68–73}$, $Fo_{74–76}$, $Fo_{77–79}$, $Fo_{80–82}$, $Fo_{83–84}$ and $Fo_{85–87}$ (Fig. 7; Supplementary Material 2). These ranges overlap the composition of olivine plateaus observed for past eruptions; however, the upper and lower limits of the observed ranges stretch toward a slightly different Fo content with respect to the past, and the compositions are on average more mafic (Figs. 6 and 7).

The sequence of normal to reverse zoning from core to rim, in association with one or multiple plateaus of distinct compositions, has led to the definition of eight dominant zoning types for the 2020–22 olivine. These are schematically illustrated in Fig. 7 and described below with their relative abundances. Type 1 are oscillatory-zoned crystals of different compositions preserving rather constant Fo concentration along the entire profile, from core to rim (10%); Type 2 are oscillatory-zoned cores with normal zoning toward the rim (16%); Type 3 has normally zoned rims with gentle slopes that gradually shift to flatter or slightly reverse profiles toward the crystal edge (15%); Type 4 is a double-step normal zoning profile characterized by a ~ 30 μm-wide intermediate zone between the core and rim at rather constant Fo composition that interrupts the normal gradient rimward (6%). Type 5 are oscillatory zoning profiles changing to reverse zoning at the crystal rim (27%); Type 6 includes oscillatory zoned cores mantled by reverse zoning that became smoother or flat toward the rims (7%); Type 7 are reverse plus normal zoning patterns, often separated by a flat zone at rather constant Fo composition (15%). In Type 7 the normal zoning pattern sometimes graduate toward the edge, becoming slightly smoother. Type 8 are more complex profiles given by the sequence of reversely zoned interiors, normally zoned rims plus reverse zoning at the crystal edge (4%).

We found that distinct core compositions preferentially associate with specific type of Fe-Mg zoning (Fig. 8). For instance, high forsteritic crystals (>Fo_{80} cores) are typically normally zoned, and occur as Type 2 (20%), Type 3 (13%) and Type 4 (6%) zoning profiles. Low forsteritic olivines (≤Fo_{80} cores) are, instead, preferentially reversely zoned, with profiles that can be mostly classified as Type 5 (27%) and Type 7 (15%) and, in minor percentage, as Type 6 and Type 8 (≤4%). Type 2 and Type 5 are the most frequent zoning types of the 2020–22 olivine assemblage, commonly characterizing crystals with cores at $Fo_{80–82}$ and $Fo_{68–73}$ respectively. The $Fo_{80–82}$ cores define the most abundant olivine population among the studied products, occurring with peak of frequency of 32%. $Fo_{77–79}$ and $Fo_{68–73}$ cores are abundant as well, forming 20% and 22% of the olivine phenocrysts, respectively. $Fo_{77–79}$ cores preferentially associate with Type 5 and Type 7 zoning (10%). The other compositional ranges, i.e., $Fo_{85–87}$, $Fo_{83–84}$, and $Fo_{74–76}$, show up in minor proportions, which are always <15% with respect to the entire spectrum of olivine cores. None of these core compositions exhibits a dominant type of zoning.

Aside from the relative abundances of specific types of olivine zoning, we noted a relationship between the temporal distribution of distinct core populations and changes of volcanic activity over the investigated period (Fig. 9). Olivine crystals of more mafic core composition (>Fo_{80}) are typically erupted during periods of intensified fountaining activity, such as in February–April and May−July 2021, during which paroxysmal eruptions occurred with average frequency of ~24 h. Volcanic samples erupted between February 16 and April 1, 2021, contain over 23% of high forsteritic (>Fo_{80}) crystals, and this percentage extends to 26% of the total analyzed assemblage when $Fo_{77–79}$ cores are included. The most mafic $Fo_{85–87}$ olivine exclusively characterizes products of this eruptive phase, forming 2% of the total olivine cargo of 2020–22. Samples related to the eruptions of May 19 − July 8, corresponding to the second phase at high eruption frequency, contain ~10% of high forsteritic (>Fo_{80}) crystals, which however exhibit maximum Fo concentration at the core of 84 mol%. More differentiated core populations (<Fo_{80} cores) distribute more randomly throughout the entire period of activity, with the major frequency on May, June and July 2021 (Fig. 9).

5.2. New thermodynamic constraints with redefinition of the magmatic environments

The compositional differences in olivine crystals of 2020–22 necessarily imply changes of parameters like pressure, temperature or composition of the environment in which olivine forms and moves through. Based on the systematic observation and distribution of six distinct Fo plateaus from core to rim, an equal number of magmatic environments have been discriminated during 2020–22, whose compositions realistically replicates the magmatic conditions at which a crystal reside within the Etnean plumbing system (Kahl et al., 2015). Given that olivine compositions are comparable to those observed in the past, we adopted the nomenclature proposed by Giuffrida and Viccaro (2017), and later resumed by subsequent studies (i.e., Cannata et al., 2018; Viccaro et al., 2019; Borzì et al., 2020; Giuffrida et al., 2021) to describe the magmatic environments in which the core and rim plateau of the olivine erupted during 2020–22 formed. Accordingly, we indicate as M_x the most primitive $Fo_{85–87}$ environment of crystallization. The environments M_{00} ($Fo_{83–84}$), M_0 ($Fo_{80–82}$), M_{1a} ($Fo_{77–79}$), M_{1b} ($Fo_{74–76}$) and M_2 ($Fo_{68–73}$) are representative, in succession, of increasingly evolved magmas. Besides the evidence of compositional continuity between one environment and the other, we can assume that each environment reflects a specific crystallization zone within the vertical-extended, yet continuous magmatic storage and transport system of Etna. This interpretation results from the observation of subsequent phases of chemical re-equilibration between discrete zones at constant Fo content that are compositionally similar. A good example is given in Fig. 7, which illustrates a Type 4 zoning profile where a Fo_{83} core plateau connects with a Fo_{81} central plateau via normal zoning, suggesting two phases of crystal growth in distinct environments before a final step of migration and differentiation prior to eruption.

Overall, the compositional ranges that define the 2020–22 environments are larger and more mafic comparable to those observed in the past, in accordance with results from whole rock and glass chemistry analyses. However, the new geochemical data provided in this study

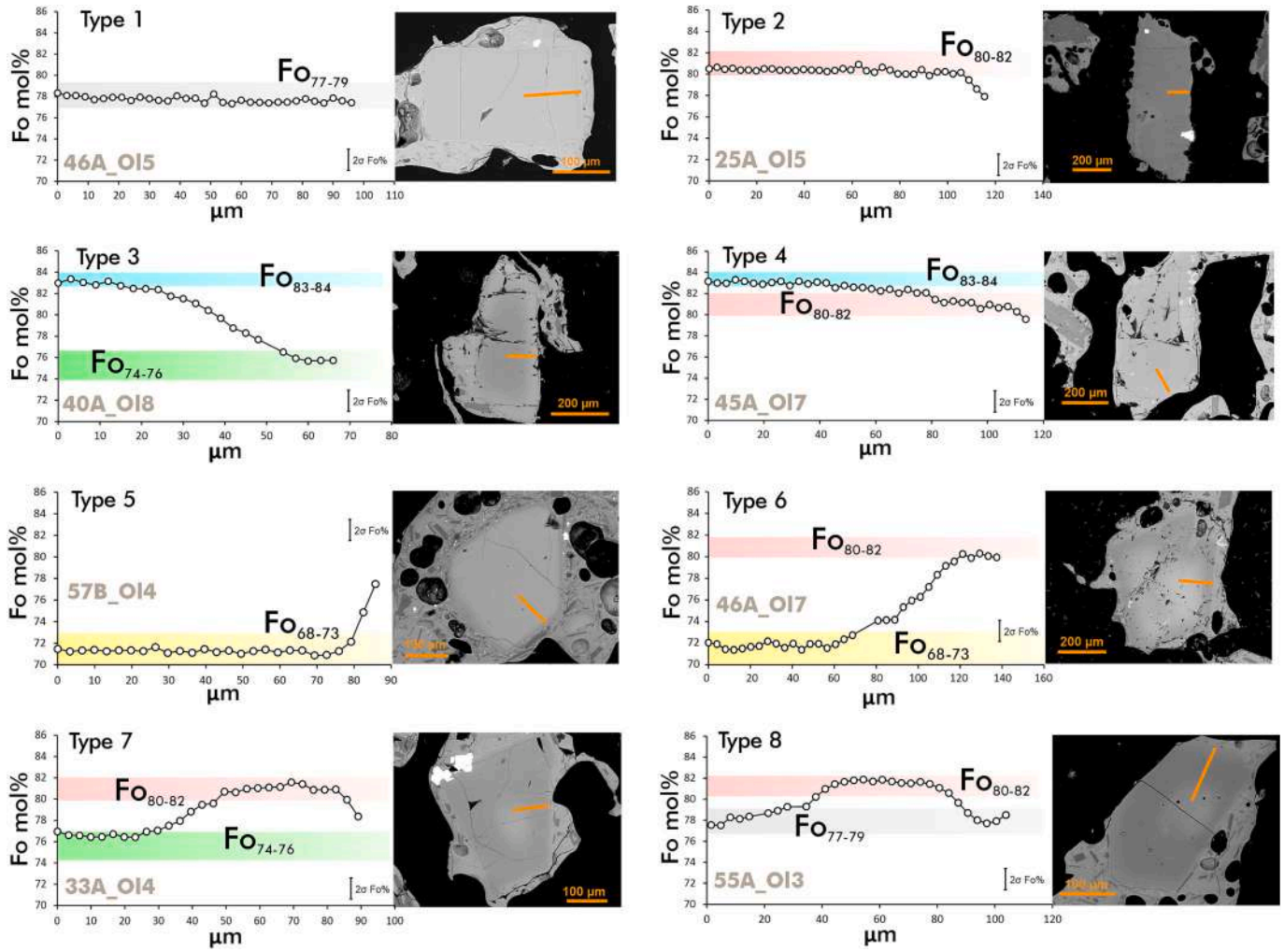

Fig. 7. Core-to-rim compositional variations and back-scattered images for representative olivine crystals that define the main zoning types observed during the 2020–22 eruptive sequence. Shaded colored bands mark Fo plateaus of equal composition observed in various crystals.

highlighted major differences in the bulk rock chemistry between volcanic products of 2020–22 and those of 2011–13, with the latter that deviate from the common trend of differentiation tracked by the 2015–22 series (Supplementary Material 1). Such variations can be interpreted as due to different crystallization conditions and fractionation of phenocryst phases over the past decade. As the magma feeding the activity during 2015–22 followed a differentiation path different from the magma of 2011–13, the physical characteristics of the magmatic environments redefined in this study are different than those previously defined by Giuffrida and Viccaro (2017) for the 2011–13 period.

We have carried out thermodynamic calculations using the rhyolite-MELTS software v. 1.2.0 (Gualda et al., 2012; Ghiorso and Gualda, 2015) in order to simulate the magmatic differentiation and physically characterize the magmatic environments in which the olivine core and rim plateaus formed. The approach adopted in this study simulates magma evolution along multiple P-T-X intervals, assuming that the differentiation occurs under crystal and fluid fractionation [i.e., separation of crystal and fluid phase (H_2O and CO_2 components) from the magmatic system], which were proved to have major impact on the crystallization paths of the Etnean magmas (Giuffrida et al., 2017). To replicate the crystallization conditions of the 2011–13 and the 2015–22 rock series, we have chosen as starting composition a primitive melt inclusion entrapped in a Fo_{84} olivine corrected for post-entrapment crystallization (PEC) and restored for the original SiO_2-H_2O-CO_2 of the system (Table 2). The selected composition derives from the dataset of Zuccarello et al. (2021) and refers to one of the most mafic melt inclusions found in olivine of the post-2011 activity. The starting pressure fixed for thermodynamic simulations (340 MPa) corresponds to the entrapment pressure of the melt inclusion as estimated by Zuccarello et al. (2021), whereas the temperature range is from 1160 °C (below the olivine liquidus temperature estimated at ~1270 °C; Giacomoni et al., 2018) down to 1065 °C in accordance with the lowest final crystallization temperatures obtained by geothermometry (1070 ± 20 °C; Kahl et al., 2015).

The adopted initial P-T conditions (340 MPa, 1160 °C) limit our ability to obtain information regarding the early magmatic crystallization in the deepest reservoirs located at pressures higher than 600 MPa, as also evidenced by thermobarometric calculations. Indeed, it is worth noting that the most primitive olivines recognized in our dataset (i.e., $Fo_{85–87}$) cannot be obtained by using this starting magma composition. On the other hand, we can characterize properly the upper-intermediate section of the feeding system, where most of the magmatic crystallization occurs (Mollo et al., 2015, 2022; Giuffrida and Viccaro, 2017). Starting from the physical and chemical conditions mentioned above, we performed multiple thermodynamic simulations of the liquid evolution along different: a) fO_2 paths (QFM-1 to QFM + 1 or NNO); b) dP/dT conditions; c) volatile budgets (H_2O from 2.5 to 1.0 wt% and CO_2 from 1800 to 300 ppm, in agreement with the volatile concentrations estimated for recent Etnean K-trachybasalts; Allard et al., 1997; Métrich

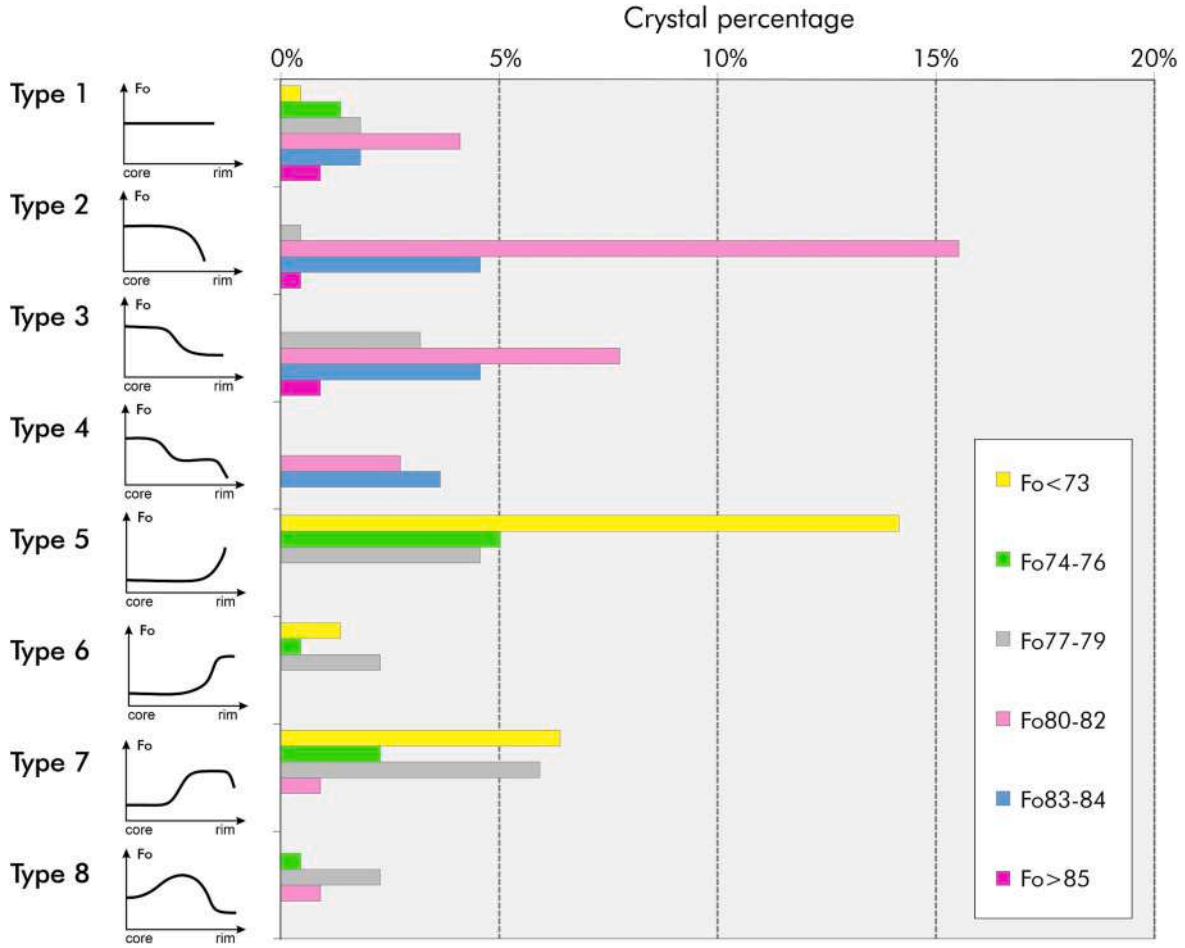

Fig. 8. Distribution of the dominant zoning types in crystals found in the 2020–22 eruptive products in relation with the olivine core compositions.

et al., 2004; Spilliaert et al., 2006; Collins et al., 2009; Zuccarello et al., 2021, 2022; see Supplementary Material 4 for a selection of the failed simulations).

The best-fit model coincides with the simulation that replicates more faithfully both the petrographic (crystallization of the olivine populations observed in natural samples) and compositional observations (whole rock geochemical trends) for the 2011–2022 volcanic rocks. The best-fit model was obtained via three steps of thermodynamic simulations across different P-T-X intervals (Fig. 10; Table 2 and Supplementary Material 4 for failed simulations regarding the three steps). The first step simulates melt differentiation in a range of temperature of 1160–1106 °C and pressure of 340–207 MPa, assuming an initial oxygen fugacity buffer QFM + 1 then shifting to QFM at 220 MPa. We obtained a good fit between the modeled liquid and the most mafic (<47.6 wt% SiO_2) rock compositions erupted between 2011 and 2022, matching well the variations in some major oxides, especially alkalis, during differentiation. Other oxides, such as FeO, TiO_2, Al_2O_3, CaO and MgO show divergences to some extent for some of the steps from the modeled trend that can be resolved assuming differential subtraction/addition of mineral phases from the system, as well as the effect of recharge and mixing events that cannot be reproduced by thermodynamic modeling using rhyolite-MELTS. Diopsidic clinopyroxene and Ti-magnetite are the first crystallizing mineral phases, followed by Fo_{84} olivine. This step produces olivine populations with compositions from Fo_{84} to Fo_{77}, but not the most mafic $Fo_{85–87}$ crystals, suggesting that the magmatic environment in which they form (i.e., M_x) develops at pressure and temperature higher than 340 MPa and 1160 °C, in accordance with the thermodynamic constraints provided by Giuffrida and Viccaro (2017).

Bearing in mind the range in core and rim plateaus for the 2020–22 olivine, we found that the $Fo_{83–84}$ composition crystallizes in a pressure range of 340–250 MPa, temperature between 1150 and 1138 °C, and fO_2 of $10^{-7.7}$ bars. Next, the modeling produces $Fo_{80–82}$ olivine at pressure of 250–235 MPa, temperature of 1138–1124 and fO_2 of $10^{-8.9}$ bar, followed by the crystallization of $Fo_{77–79}$ olivine between 235 and 178 MPa, corresponding to magmatic temperatures of 1120–1100 °C and fO_2 of $10^{-9.7}$ bars (Fig. 11). During differentiation, the redox conditions were modified from QFM + 1 to QFM to allow the crystallization of $Fo_{77–79}$ olivine. These thermodynamic constraints are considered representative of the M_{00}, M_0 and M_{1a} magmatic environments, respectively (Fig. 11). These environments show similar volatile budgets, as the H_2O content increased a little from 2.5 to 2.7 wt%, while CO_2 decreased from 1800 to 1100 ppm as the differentiation proceeds. The set of thermodynamic variables defining the environments M_{1b} ($Fo_{74–76}$) and M_2 ($Fo_{68–73}$) were constrained at lower P-T values via two separated simulations (Step 2 and Step 3 in Fig. 11), both performed at P = 207–60 MPa and T = 1106–1065 °C. The two simulations started from the same melt composition, reported in Table 2, which derives from the Step 1 of differentiation at temperature of 1106 °C, pressure of 207 MPa and 2.6 wt% of water. Step 2 and Step 3 were designed to simulate two different processes of liquid evolution matching the divergent compositions of the 2011–13 and 2015–22 rock suites, respectively. However, the production of such more evolved compositions required changing the redox conditions of the system with respect to Step 1, from QFM to QFM-1, as well as the adoption of differentiate dP/dT conditions and water concentrations to account for the major differences in the CaO, FeO_{tot}, TiO_2 and alkalis between the two rock suites (Fig. 10; Table 2). Specifically, the differentiation path

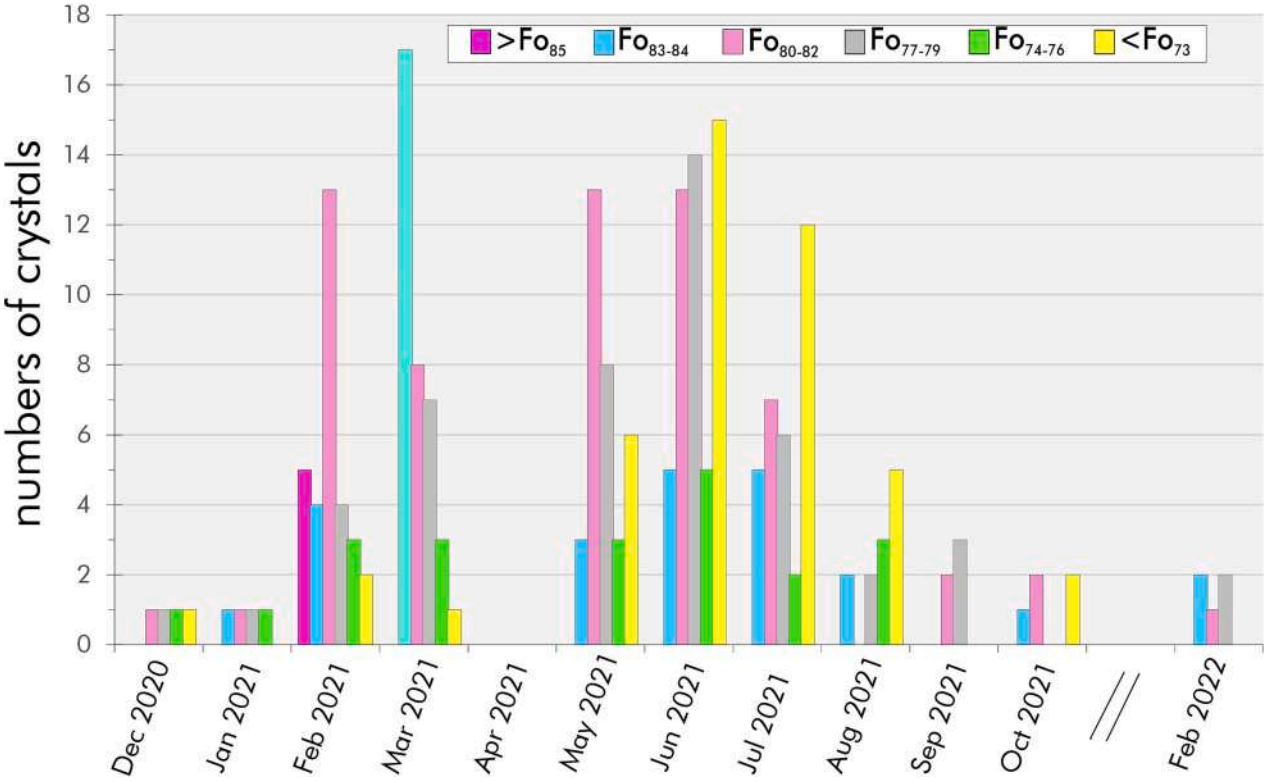

Fig. 9. Temporal variation of the olivine core populations erupted between December 2020 and February 2022.

Table 2
Major oxide starting compositions (wt%) used for the three-steps modeling with rhyolite-MELTS v. 1.2.0. Temperature and pressure intervals, along with dP/dT and oxygen buffers are shown for each step.

	Starting melt compositions		
Conc. wt%	Step 1	Step 2	Step 3
SiO_2	46.1	47.8	47.8
TiO_2	1.71	1.59	1.59
Al_2O_3	15.9	16.6	16.6
FeO_{tot}	10.4	8.75	8.75
MnO	0.10	0.10	0.10
MgO	7.58	5.70	5.70
CaO	10.1	10.6	10.6
Na_2O	3.27	3.56	3.56
K_2O	1.72	1.87	1.87
P_2O_5	0.53	0.58	0.58
H_2O	2.50	2.00	2.60
CO_2	0.17	0.11	0.11
T (°C)	1160–1106	1106–1065	1106–1065
P (MPa)	340–207	207–60	207–60
dP/dT	39	37	49
fO_2 buffer	QFM + 1 / QFM	QFM-1	QFM-1

simulated in Step 2 reproduces the rock composition of 2011–13 by subtracting 0.6 wt% of water from the system with respect to its initial concentration (originally 2.6 wt% from Step1). Step 3 matches the rock compositions of 2015–22 starting from 2.6 wt% of water, but assuming higher dP/dT value compared to Step 2 (Fig. 10; Table 2). The good fit provided by the two models suggests that the compositional differences between the two rock suites can be reasonably ascribed, at least in part, to a different degree of melt hydration and some differences in the kinetics of migration and cooling (dP/dT) that must have been changed since 2015, with consequent impact on the crystallization path of the Etnean magmas. In detail, we observed for the 2015–22 series a larger range of crystallization pressures for the $Fo_{74–76}$ and $Fo_{68–73}$ olivines if compared to the 2011–2013 series (Fig. 11). Thermodynamic constraints for the recent 2020–22 eruptive cycle suggest that the $Fo_{74–76}$ compositions (associated to the environment M_{1b}) develops at pressure of 140–70 MPa, temperature of 1096–1080 °C and fO_2 of $10^{-10.5}$ (Fig. 11). The evolved compositions at $Fo_{68–73}$ related to the environment M_2 can be reproduced only at very low pressure (<60 MPa), temperature (<1080 °C) and fO_2 of $10^{-10.7}$, which corresponds to the shallowest part of the feeding system, extending from depth of ~2 km below the summit to the surface (Fig. 11).

6. Histories of magmatic injections, residence and remobilization over the 2020–22 eruptive cycle

Thermodynamic simulations allowed the definition of the physical and chemical characteristics of the crystallization environments in which the plateaus observed at the olivine core and rim formed. In Section 5.1, we have illustrated how compositional plateaus in olivines found in the 2020–22 products connect one to the other by zoned profiles, normal or reverse, and how the compositional variation from core to rim defines various zoning types that are recurrent over the studied period (Figs. 7 and 8; Supplementary Material 2). Chemical zoning in magmatic crystals typically originates from the combined effects of crystal growth plus diffusion that activates in response of chemical contrasts. In this context, the observed Fo changes can be accomplished either by the crystal (plus the associated melt) physically moving from one environment to a shallower and more evolved one or, in alternative, by the host environment itself changing composition due to mafic recharge or crystallization/crystal fractionation. While decreasing Fo concentration and the development of normal zoning patterns would be likely produced by melt differentiation or rapid crystal incorporation in more evolved environments, increasing Fo concentration and reverse zoning would be expected in case of mafic recharge.

Since any plateau identifies an olivine growth zone developing under a defined P-T-X-fO_2 interval, we have assumed that changes in the zoning pattern from one plateau to another are equivalent to the transfer of the crystal from one environment to another.

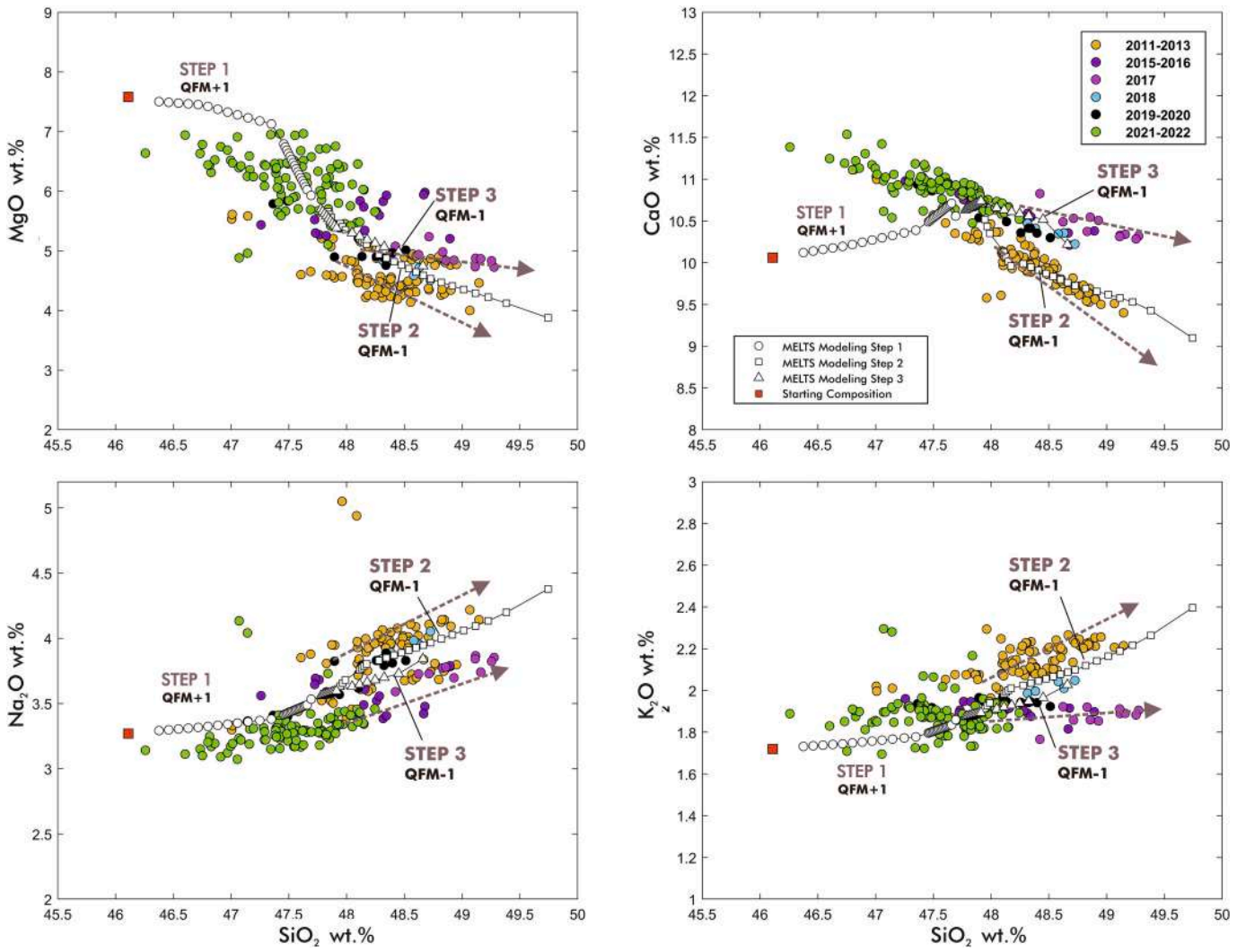

Fig. 10. Chemical evolution of the melt (white symbols) resulting from rhyolite-MELTS simulations, considering differentiation driven by crystal plus fluid fractionation. The data best fit with major oxides of whole rocks erupted during the 2011–22 period was obtained via three steps of modeling: the first step matches the major oxide compositions of the less evolved rocks of the decade. The second and the third steps match the compositional variations of the 2011–13 and the 2015–22 rock series respectively.

The multiple types of zoning characterizing the 2020–22 olivine crystals reflect a complex migration history of magmas feeding the recent paroxysmal sequence, an history made of multi-stage magmatic injections, residence and re-mobilization that involved end-members from six magmatic environments. The frequency of core compositions and the frequency of connections between successive compositional plateaus is a clue of the relative frequency with which individual environments were activated and a pathway between different environments was used. Fig. 12 illustrates through system analysis diagrams (cf. Kahl et al., 2011, 2015) these connections between environments as resulted from the analysis of the olivine zoning patterns in products erupted throughout the 2011–22 period. Crystals that are quite homogeneous without significant compositional zoning are also displayed in the plots to illustrate direct routes of migration from the host environment to the surface.

By using the systems analysis approach, we found for the 2020–22 eruptive sequence a prevalent connection between the environments M_0 ($Fo_{80–82}$) and M_{1a} ($Fo_{77–79}$), which is evident for both the eruptive phases of December 2020 – April 2021 and May 2021 – February 2022 (Fig. 12). M_0 and M_{1a} also represent the environments where the majority of the olivine cores have formed (core compositions between Fo_{77} and Fo_{82} constitute 52% of the total assemblage analyzed in this study; Fig. 6). These environments define a main interval of the feeding system between 250 and 178 MPa that appears as the principal ponding zone for magmas uprising from the deepest, mafic environments M_x (>Fo_{85}) and M_{00} ($Fo_{83–84}$). On the other hand, the M_0 and M_{1a} magmas continuously supply more evolved environments such as M_{1b} and M_2.

Main differences in the distribution of the olivine core compositions and associated zoning profile between the two eruptive phases of the whole paroxysmal sequence imply that some changes have occurred in the dynamics of the plumbing system over time (Fig. 12; Supplementary Material 2). In olivines of the first eruptive phase, we observe two dominant connection patterns M_{00}-M_0 and M_0-M_{1a}, with the core population at Fo ≥ 83 exclusively present in products erupted between mid-February and mid-March 2021. Although $Fo_{85–87}$ crystals are subordinate, some patterns connecting the environments M_x-M_{00} and M_x-M_0 are observed, and these are exclusive of the February 2021 olivines. It is worth noting that some crystals coming from the mafic M_x, M_{00} and M_0 environments also record direct connections with the surface without further steps of storage in other environments. Overall, the connection patterns between the shallowest environments, such as M_{1a}-M_{1b}-M_2 are much less frequent when compared with the M_{00}-M_0-M_{1a} pathway (Fig. 12; Supplementary Material 2). In contrast, olivine crystals from the second phase of the paroxysmal sequence present abundant evidence

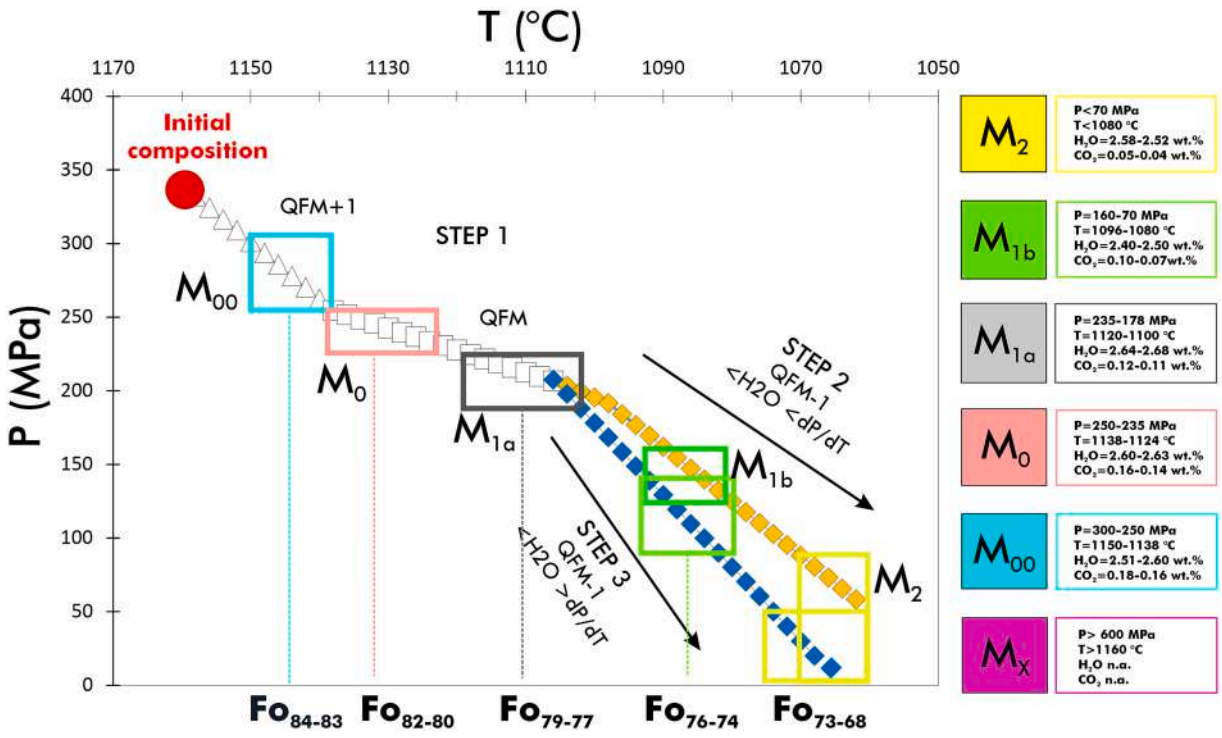

Fig. 11. Changing composition of the melt as a function of pressure and temperature with indication of the thermodynamic variables that define the six magmatic environments (M) detected at Mt. Etna based on the olivine core compositions (colored boxes). Note that the pressure and temperature shown for M_{1a} (green box) and M_2 (yellow box) refer to the entire range of crystallization pressure and temperature constrained through the Step 2 and the Step 3 of modeling. (For interpretation of the references to colour in this figure legend, the reader is referred to the web version of this article.)

of magma movements in the upper plumbing system, following the pathway M_{1a}-M_{1b}-M_2, with clear prevalence of the M_{1a}-M_2 patterns since July 2021 (Fig. 12; Supplementary Material 2). The connection M_0-M_{1a}, however, confirms itself as the dominant path that crystals record in this period. Besides the main connection routes, several crystals record early stage of growth in M_{00} and the subsequent passage in more evolved reservoirs (from M_0 to M_2). However, the appearance of M_{00} is somewhat scattered across the period, being limited to crystals emitted during separated eruptive phases (e.g., during May 19–26, June 19–26, July 2–6, 2021) or discrete episodes of lava fountains (e.g., in July 31, August 29 and October 23, 2021, and February 10, 2022; Supplementary Material 2). These features can be interpreted as periodic ascent of mafic magma batches from 250 to 300 MPa that pushed upward the magmas residing at shallow levels, fueling a mechanism of multi-level magma intrusion and remobilization across the Mt. Etna plumbing system. This interpretation cannot be applied to the first phase of the paroxysmal sequence, for which the overall dataset suggests significant refilling of the plumbing system between 178 and 250 MPa (~5–7 km below the summit) with recharging magmas ascending from deep regions (>10 km), at least in the period February 16–March 19, 2021. In the context of the previous decade, observations for 2020–22 sequence are in line with what the 2011–13 and 2015–16 paroxysmal sequences suggest, where the rapid mobilization of the deepest and more mafic reservoirs, such as the M_{00} and M_x, pressurized the intermediate plumbing system, then triggering subsequent episodes of transfer, intrusion, and residence involving more differentiated magmatic end-members, mainly M_{1b} and M_2 (Fig. 12). Substantial mobilization of partially degassed magmas residing at low crustal pressure (< 235 MPa) is evident since the end of the 2016 eruptions at VOR (Fig. 12), resulting in over four years of effusive-to-low explosivity volcanic phenomena.

In addition to the identification of the migration paths, we performed Fe—Mg diffusion modeling to assess the timescales over which the crystals of the 2020–22 eruptive sequence (and their associated melts) have been transferred between the environments and reconstructed the timeline of the episodes of magmatic intrusions for different sections of the plumbing system prior to the eruption (Supplementary Material 3). We used the method of finite differences (Costa et al., 2008) for modeling the diffusive relaxation of compositional zoning profiles in 71 olivines from the 2020–22 eruptive record. Most of the analyzed crystals did not fulfill the established criteria for robust time estimates (Costa and Chakraborty, 2004; Costa et al., 2008; Shea et al., 2015a, 2015b) and were, therefore, not modeled by diffusion. The criteria for the choice of olivine crystals and concentration profiles for the modeling, the input parameters and reliability of the results are reported in the Appendix of this study. We have modeled normal and reverse zoning profiles connecting olivine core and rim of distinct compositions, and therefore associated to different environments. The timescales we obtained refers to the total time a given crystal spends into the plumbing system after entering a final magmatic environment prior to eruption. A summary of the obtained timescales with indication of the pathway between environments as recorded from the modeled zoning profiles is provided in Table 3. The array of diffusion timescales calculated from crystals of subsequent eruptions gave us the opportunity to reconstruct the sequence of episodes of magmatic intrusion feeding the 2020–22 volcanic activity at SEC (Figs. 13-14). The observed distribution of timescales vary from a minimum of 2 days to a maximum of 8 months, with the majority (~72%) of the obtained times being shorter than 2 months, in good agreement with results from other recent Etna eruptions (Viccaro et al., 2016b, 2019; Giuffrida and Viccaro, 2017; Cannata et al., 2018; Borzì et al., 2020; Giuffrida et al., 2021).

The time estimates for olivines emitted during the first phase of the paroxysmal sequence suggest two main phases of mafic recharge into the M_{1a} and M_0 environments, following the ascent of the M_x and M_{00} magmas from deepest reservoirs (Fig. 13). The first evidence of the ascent of M_{00} goes back to ~5 months before the first paroxysmal episode on December 13–14, 2020. However, other magma pulses of comparable composition are detected later. The first important recharging phase coincides with the period between mid-November and the first week of

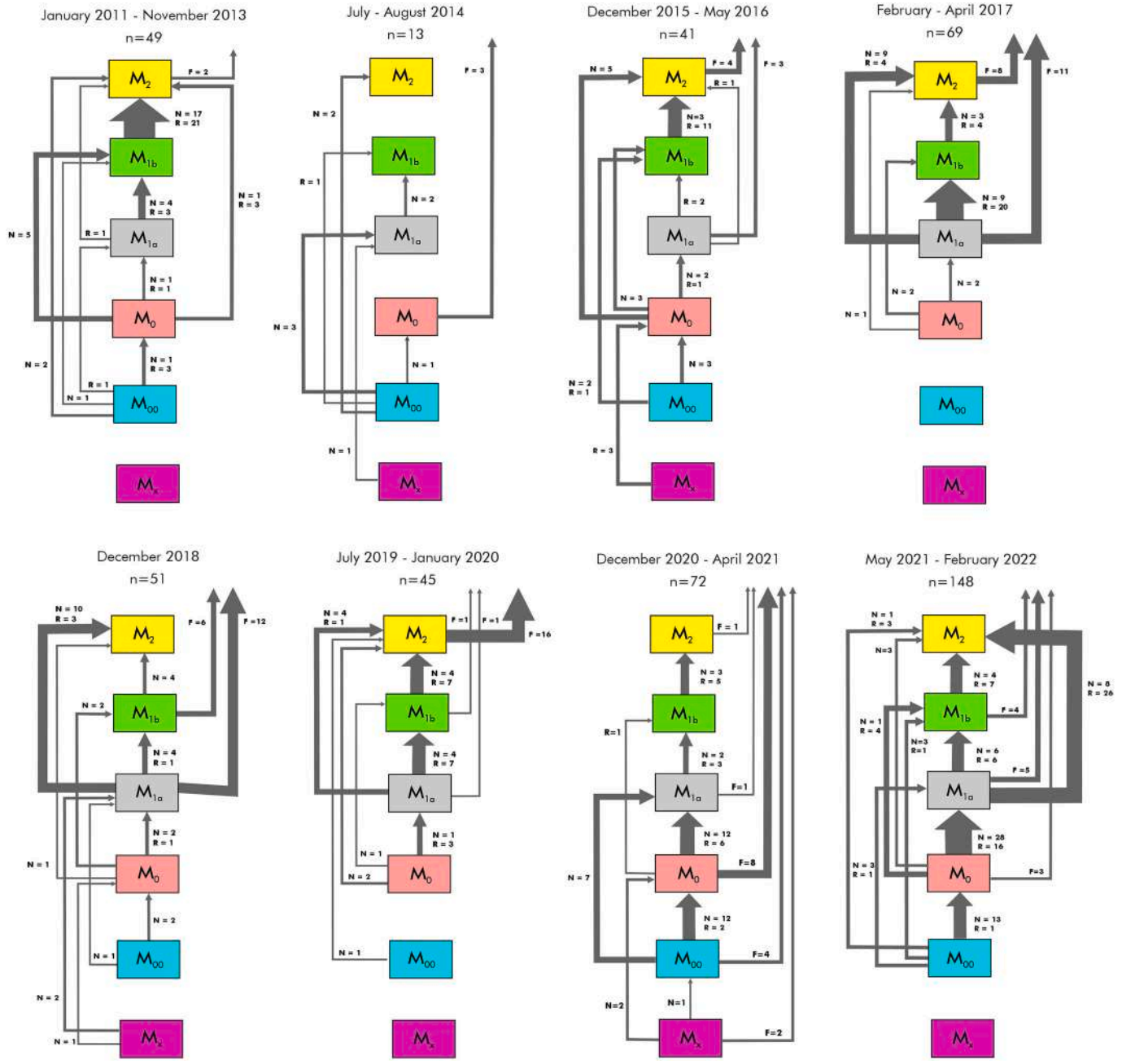

Fig. 12. System analysis diagrams illustrating the connections between magmatic environments (colored boxes) and the pathways of magma migration (black arrows) during the 2011–22 period. Thickness of the arrows is proportional to the number of connections between environments as defined from the observed olivine zoning patterns (the corresponding numbers of connections are given next to each arrow), while the arrow directions mimic the direction of magma movement. For each sub-period the total number (n) of crystals has been reported; N indicates connections resulting by normal zoning, while R those by reverse zoning.

December 2020, just before the beginning of the paroxysmal sequence (Fig. 13). In this time interval, our data indicate replenishment of M_{1a} in response of dominant magma movements along the pathways M_{00}-M_{1a}, M_{00}-M_0 and M_0-M_{1a}. This process must have produced almost contemporaneous melt injections in magmatic reservoirs at shallow depths (e.g., M_2) prompting the onset of volcanic activity on December 13–14, 2020. Interestingly, our evidence is well supported by other petrological models (Corsaro and Miraglia, 2022) and monitoring data (e.g., increase of the CO_2 flux, as evidenced since the multidisciplinary INGV Etna weekly report 48/2020 available at www.ct.ingv.it) and the concomitant occurrence of deep (>12 km b.s.l.) and shallow (<3 km b.s.l.) clusters of earthquakes; De Gori et al., 2021)]. The second, notable phase of deep recharge coincides with the first half of January 2021 (January 4–13; Fig. 13). In this period, the most mafic M_x magma rose up from a deep zone of the plumbing system (>16 km b.s.l. based on thermodynamic calculations in section 5.2) and started to intrude the intermediate reservoirs M_0 and M_{1a}. The migration of the M_x magma along the observed pathways M_x-M_0 and M_x-M_{1a} was found to occur in short timescales of 8–43 days. As we have not further indication of subsequent intrusion and storage in reservoirs shallower than M_{1a}, we can assume that once reaching the M_{1a} reservoir the magma migrated directly to the surface, leading to the activity of January 18, 2021. Just a month later the first detection of M_x, a sequence of short-lasting episodes of melt injections across the M_{1a}, M_{1b}, M_2 reservoirs are evident. Such episodes are recurrent during the paroxysmal activity of February–March 2021, and generally occur 3–16 days before each eruption (Fig. 13).

Table 3
Diffusion modeling results for olivine crystals in products erupted during the 2020–22 paroxysmal sequence at the South East Crater of Mt. Etna. Timescales (days) and relative uncertainties (±σ) were calculated for distinct zoned portions of an olivine crystal (n: normal; r: reverse), each indicating a given connection between two subsequent magmatic environments (M_i). Thermodynamic parameters used for modeling the diffusive relaxation of the observed zoned profiles are also shown.

Eruption date	Crystal	T (°C)	P (MPa)	fO_2 (bars)	M_i	Δt ± σ
Dec 13–14, 2020	Ol1_1B	1110	207	$10^{-9.73}$	M0-M1a (n)	33 ± 7
Jan 18, 2021	Ol1_4A	1110	207	$10^{-9.73}$	M00-M1a (n)	185 ± 112
Feb 16, 2021	Ol2_5B	1110	207	$10^{-9.73}$	M0-M1a (n)	8 ± 11
	Ol5_5B	1110	207	$10^{-9.73}$	M0-M1a (n)	32 ± 10
	Ol1_5B	1133	242	$10^{-8.92}$	Mx-M0 (n)	43 ± 8
Feb 17–18, 2021	Ol2_6c	1110	207	$10^{-9.73}$	M0-M1a (n)	5 ± 3
	Ol2_6A	1088	115	$10^{-10.75}$	M2-M1b (r)	6 ± 4
Feb 19, 2021	Ol3_7B	1088	115	$10^{-10.51}$	M0-M1b (n)	76 ± 40
Feb 20–21, 2021	Ol3_8B	1110	207	$10^{-9.73}$	M0-M1a (n)	36 ± 22
	Ol5_8B	1088	115	$10^{-10.51}$	M0-M1b (n)	10 ± 6
Feb 22–23, 2021	Ol1_9Ab	1110	65	$10^{-9.73}$	M2-M1a (r)	5 ± 3
	Ol3_9Ab	1133	207	$10^{-8.92}$	M1a-M0 (r)	231 ± 132
	Ol3_9Ab	1088	115	$10^{-10.51}$	M0-M1b (n)	62 ± 24
Feb 24, 2021	Ol3_10A	1110	115	$10^{-9.73}$	M1b-M1a (r)	3 ± 2
	Ol1_10B	1110	207	10–9.73	M00-M1a (n)	42 ± 25
Feb 28, 2021	Ol2_11Bb	1144	242	$10^{-8.92}$	Mx-M0 (n)	8 ± 4
Mar 2, 2021	Ol2_12A	1110	207	$10^{-9.73}$	M00-M1a (n)	99 ± 60
	Ol1_12B	1133	242	$10^{-8.92}$	M00-M0 (n)	53 ± 30
Mar 4, 2021	Ol2_13A	1110	207	$10^{-9.73}$	M0-M1a (n)	11 ± 7
Mar 7, 2021	Ol1_14B	1088	65	$10^{-10.51}$	M2-M1b (r)	6 ± 4
	Ol2_14B	1133	207	$10^{-8.92}$	M1a-M0 (r)	7 ± 4
	Ol3_14C	1133	207	$10^{-8.92}$	M1a-M0 (r)	16 ± 9
Mar 9–10, 2021	Ol2_15B	1088	65	$10^{-10.51}$	M2-M1b (r)	5 ± 3
Mar 14–15, 2021	Ol2_17B	1088	65	$10^{-10.51}$	M2-M1b (r)	30 ± 18
Mar 19, 2021	Ol1_19B	1110	207	$10^{-9.73}$	M0-M1a (n)	2 ± 1
Mar 23–24, 2021	Ol1_20B	1110	65	$10^{-9.73}$	M2-M1a (r)	7 ± 4
Mar 31-Apr 1, 2021	Ol3_21C	1144	242	$10^{-7.74}$	M0-M00 (r)	83 ± 47
	Ol3_21C	1133	242	$10^{-8.92}$	M00-M0 (n)	8 ± 4
	Ol4_21C	1088	65	$10^{-10.51}$	M2-M1b (r)	120 ± 73
May 19, 2021	Ol2_22A	1088	115	$10^{-10.51}$	M0-M1b (n)	5 ± 3
	Ol6_22A	1088	115	$10^{-10.51}$	M0-M1b (n)	47 ± 28
May 21, 2021	Ol3_23A	1088	115	$10^{-10.51}$	M0-M1b (n)	15 ± 9
	Ol8_23A	1133	207	$10^{-8.92}$	M1a-M0 (r)	54 ± 31
	Ol8_23A	1110	207	$10^{-9.73}$	M0-M1a (n)	28 ± 12
	Ol9_23A	1133	115	$10^{-8.92}$	M1b-M0 (r)	7 ± 4
May 22, 2021	Ol3_24A	1110	207	$10^{-9.73}$	M0-M1a (n)	63 ± 37
May 24, 2021	Ol3_25A	1144	242	$10^{-8.92}$	M00-M0 (n)	57 ± 33
	Ol5_25A	1110	207	$10^{-9.73}$	M0-M1a (n)	3 ± 2
May 26, 2021	Ol2_28B	1110	65	$10^{-9.73}$	M2-M1a (r)	26 ± 17
May 28, 2021	Ol1_31B	1133	207	$10^{-8.92}$	M1a-M0 (r)	74 ± 36
Jun 2, 2021	Ol3_33A	1110	115	$10^{-9.73}$	M1b-M1a (r)	3 ± 1
	Ol4_33A	1133	115	$10^{-8.92}$	M1b-M0 (r)	32 ± 13
Jun 16, 2021	Ol5_37A	1088	115	$10^{-10.51}$	M0-M1b (n)	61 ± 37
Jun 19, 2021	Ol2_39B	1110	207	$10^{-9.73}$	M0-M1a (n)	92 ± 54
	Ol5_39B	1110	207	$10^{-9.73}$	M0-M1a (n)	26 ± 15
Jun 20, 2021	Ol1_40A	1110	65	$10^{-9.73}$	M2-M1a (r)	133 ± 78
	Ol6_40A	1110	65	$10^{-9.73}$	M2-M1a (r)	59 ± 35
	Ol9_40A	1110	65	$10^{-9.73}$	M2-M1a (r)	124 ± 73
Jun 22, 2021	Ol2_41B	1133	207	$10^{-8.92}$	M1a-M0 (r)	200 ± 113
	Ol7_41B	1110	65	$10^{-9.73}$	M2-M1a (r)	7 ± 4
Jun 23, 2021	Ol1_43A	1088	65	$10^{-10.51}$	M2-M1b (r)	10 ± 6
	Ol4_43A	1133	65	$10^{-8.92}$	M2-M0 (r)	8 ± 4
	Ol10_43A	1110	65	$10^{-9.73}$	M2-M1a (r)	7 ± 4
Jun 25, 2021	Ol1_45A	1088	65	$10^{-10.51}$	M2-M1b (r)	126 ± 76
	Ol1_45A	1075	65	$10^{-10.75}$	M1b-M2 (n)	11 ± 4
	Ol5_45A	1088	115	$10^{-10.51}$	M0-M1b (n)	60 ± 31
	Ol7_45A	1144	242	$10^{-8.92}$	M00-M0 (n)	225 ± 132
Jun 26, 2021	Ol2_47B	1133	242	$10^{-8.92}$	M00-M0 (n)	59 ± 36
Jun 28, 2021	Ol1_49C	1110	207	$10^{-9.73}$	M0-M1a (n)	14 ± 8
	Ol3_49C	1110	207	$10^{-9.73}$	M0-M1a (n)	44 ± 26
	Ol4_49C	1133	207	$10^{-8.92}$	M1a-M0 (r)	39 ± 22
Jul 1–2, 2021	Ol4_50C	1133	207	$10^{-8.92}$	M1a-M0 (r)	28 ± 16
Jul 4, 2021	Ol7_51B	1110	207	$10^{-9.73}$	M0-M1a (n)	73 ± 45
Jul 6, 2021	Ol2_52A	1133	207	$10^{-8.92}$	M1a-M0 (r)	216 ± 122
Jul 8, 2021	Ol8_53B	1110	65	$10^{-9.73}$	M2-M1a (r)	9 ± 5
Jul 14, 2021	Ol1_54C	1110	65	$10^{-9.73}$	M2-M1a (r)	40 ± 24
	Ol2_54C	1110	65	$10^{-9.73}$	M2-M1a (r)	10 ± 6
	Ol5_54C	1110	65	$10^{-9.73}$	M2-M1a (r)	66 ± 39

(*continued on next page*)

Table 3 (*continued*)

Eruption date	Crystal	T (°C)	P (MPa)	fO_2 (bars)	M_i	$\Delta t \pm \sigma$
Jul 31, 2021	Ol7_56A	1110	207	$10^{-9.73}$	M0-M1a (n)	10 ± 6
	Ol11_56A	1133	242	$10^{-8.92}$	M00-M0 (n)	12 ± 9
	Ol12_56C	1110	65	$10^{-9.73}$	M2-M1a (r)	27 ± 16
Sep 21, 2021	Ol1_59B	1133	207	$10^{-8.92}$	M1a-M0 (r)	61 ± 35
	Ol2_59B	1110	207	$10^{-9.73}$	M0-M1a (n)	54 ± 32
	Ol3_59B	1110	207	$10^{-9.73}$	M0-M1a (n)	47 ± 27
Feb 10, 2022	Ol2_61A	1110	207	$10^{-9.73}$	M00-M1a (n)	193 ± 103

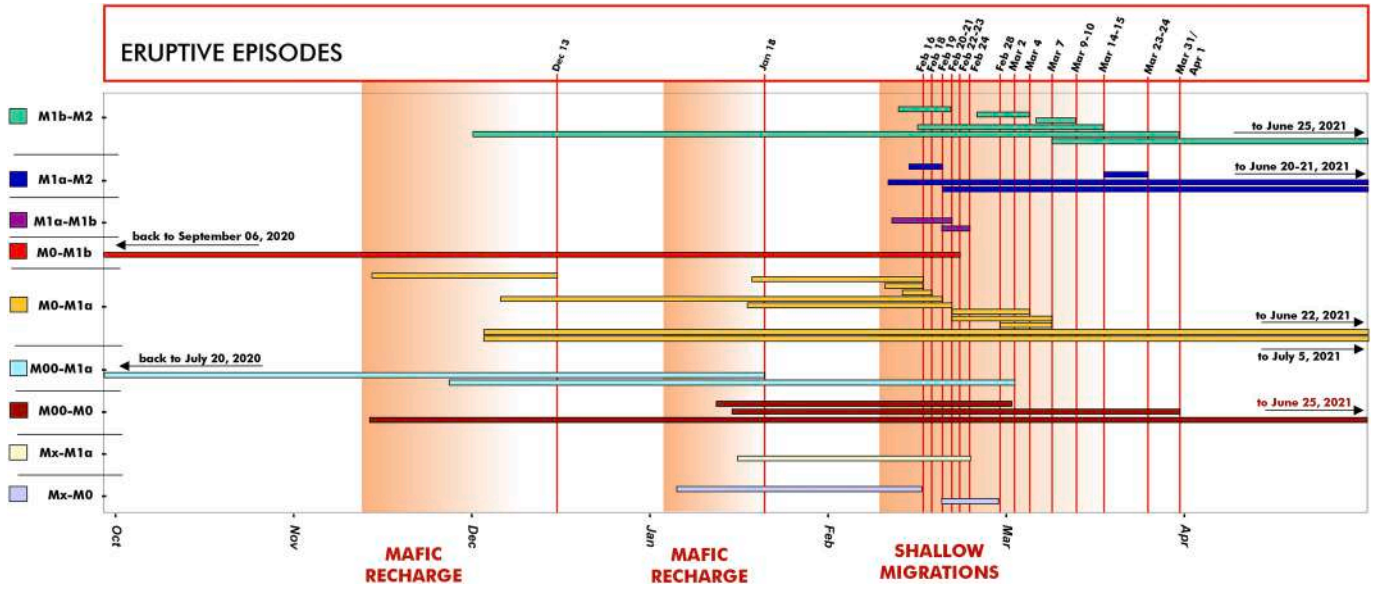

Fig. 13. Timeline of the volcanic activity at SEC from December 13, 2020 to April 1, 2021, with indication of the key episodes of magmatic intrusion. The eruptive episodes (vertical red lines) are shown together with the main magmatic intrusive episodes (red-shaded colored areas) involving distinct environments (M). Horizontal colored bars indicate the time of intrusion in a given environment as determined from olivine diffusion. Black arrows on the left refer to the timing of magmatic intrusions recorded before October 1, 2020. Black arrows on the right refer to the dates of eruption of crystals emitted after May 1, 2021. (For interpretation of the references to colour in this figure legend, the reader is referred to the web version of this article.)

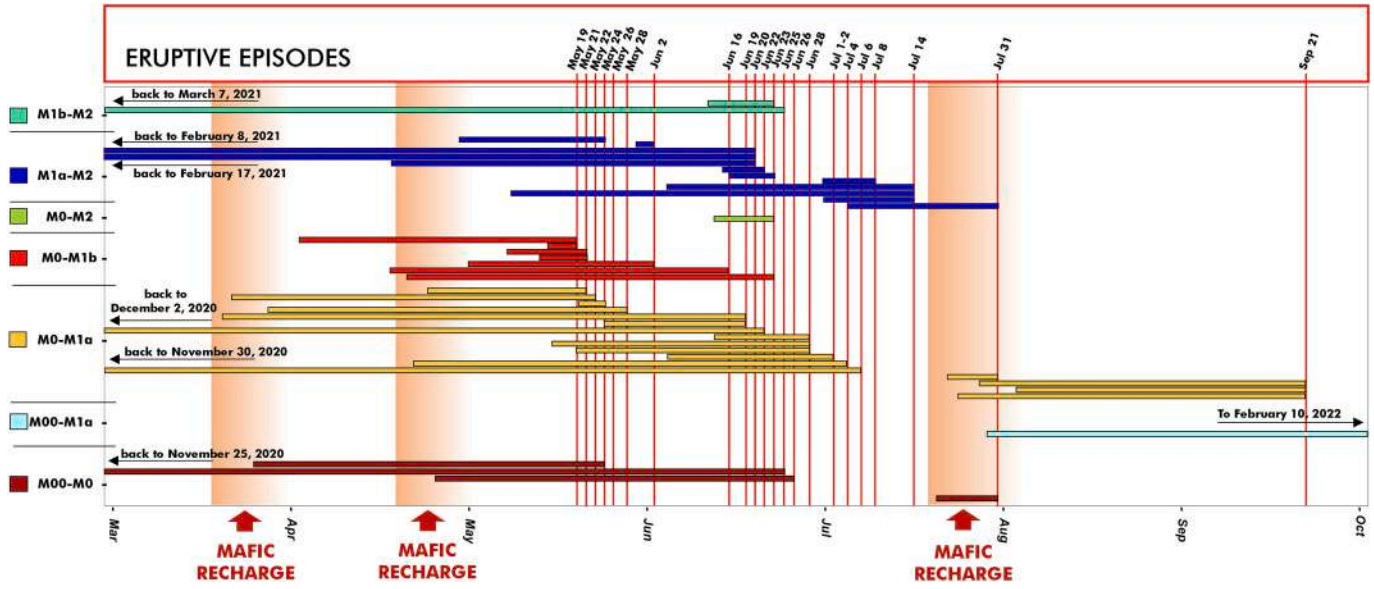

Fig. 14. Timeline of the volcanic activity at SEC from May 19 to September 21, 2021, with indication of the key episodes of magmatic intrusion. The eruptive episodes (vertical red lines) are shown together with the main magmatic intrusive episodes (red-shaded colored areas) involving distinct environments (M). Horizontal colored bars indicate the time of intrusion in a given environment as determined from olivine diffusion. Black arrows on the left refer to the timing of magmatic intrusion recorded before March 1, 2021. Black arrows on the right indicate the dates of eruption of crystals emitted after October 1, 2021. (For interpretation of the references to colour in this figure legend, the reader is referred to the web version of this article.)

Starting from May 19, our model indicates periodic ascent of the M_{00} magma that migrated upwards in 12–225 days, preferentially following the M_{00}-M_0 path (Fig. 14). We observed three M_{00} magma pulses coinciding with the second half of March, April and July 2021, respectively. Each of the observed episodes of mafic intrusion is followed by subsequent events of magma transport toward reservoirs located at increasingly lower pressures. These features let us figure out that mechanisms of multistage magma transport were going on, pushing upward with time the magma residing in the upper plumbing system and leading to the resumption of volcanic activity on May 19, 2021.

7. How the plumbing system of Mt. Etna worked during a decade of volcanic activity

The 2020–22 paroxysmal sequence at Mt. Etna captured great interest of the volcanological community due to the extraordinary explosive activity observed at the volcano, which can be considered among the most energetic of the entire last decade. In this review, we have contextualized this exceptional eruptive sequence within the framework of the post-2011 volcanic activity at Mt. Etna, producing a comprehensive picture of the spatial and temporal dynamics of magma storage and transfer across the whole volcano plumbing system.

Looking at the past, the 2020–22 paroxysmal sequence displays important resemblances with trends of storage and transfer observed for other previous periods characterized by paroxysmal eruptions. Alike to the 2011–13, significant phases of deep recharge make peculiar the early periods of the eruptive sequence, with activation of the deepest magmatic environments and mobilization of the most mafic magmas upward to shallower levels. Replenishment by these mafic magmas through time produced progressive permeation and substitution into the shallow plumbing system. Indeed, the later periods of volcanic activity for both the 2011–13 and 2020–22 sequences bear evidence of predominant activation of the shallow magmatic environments, with only sporadic recharging phases from the deepest environments occurred during the paroxysmal sequences.

If spatial dynamics of the last paroxysmal sequence closely resemble those of the 2011–13 period, the same is not true for the temporal development of the events. Indeed, timescales of magma movements associated to the preparation of the 2020–22 paroxysmal eruptions are definitely faster than those registered during the 2011–13 for almost all the connections between magmatic environments (days to weeks vs. weeks to months, respectively), presenting conversely great similarities with timescales of transfer leading to the powerful eruptions at the Voragine crater during 2015–16 (days to weeks). Although these last events are transitory within the entire 2011–2022 period, being interposed between the 2014 and 2017–2020 periods of dominantly effusive activity, they can be assumed as a benchmark in the recent Mt. Etna volcanism, since it is markedly evident that a profound change in the magma transfer ability across the whole plumbing system occurred from that moment on. Dynamics leading to the 2020–22 paroxysmal eruptions can be therefore viewed as hybrid with respect to those observed during the 2011–13 and 2015–16 sequences, resembling the spatial activation through time of magmatic environments like during the first sequence, but with faster transfers compatible with the second one. This current trend allows significant magma volumes entering into the deep plumbing system to be drained over shorter times if compared to past eruptions. Clear corroboration of this statement can be found analyzing the erupted volumes throughout the whole decade. The total volume of magma erupted in the period 2011–15 (excluding the paroxysmal eruptions at Voragine) has been estimated at $\sim 106 \times 10^6$ m^3 (Ganci et al., 2018), with $\sim 80 \times 10^6$ m^3 emitted during the 44 lava fountaining episodes of 2011–13 (Ganci et al., 2018) and the remnant $\sim 26 \times 10^6$ m^3 during the effusive activity of 2014–15. The eruptions at Voragine poured out $\sim 10 \times 10^6$ m^3 of magma on 2015 (Bonaccorso and Calvari, 2017) and $\sim 4.7 \times 10^6$ m^3 on 2016 (Ganci et al., 2019). Interestingly, the total volume of magma erupted in the period 2017–22 can be conservatively estimated at $\sim 126 \times 10^6$ m^3 (Cappello et al., 2019; Calvari et al., 2020; De Beni et al., 2021; Ganci et al., 2023), with $\sim 108 \times 10^6$ m^3 emitted during the 62 lava fountaining episodes of 2020–22 (Ganci et al., 2023) and $\sim 18 \times 10^6$ m^3 emitted during the effusive activity of 2017–19 at the SEC [namely: $11.3 \pm 2.8 \times 10^6$ m^3 in 2017 (Cappello et al., 2019); $\sim 2.8 \times 10^6$ m^3 for the lateral eruption of Christmas 2018 (Calvari et al., 2020); $\sim 4.4 \times 10^6$ m^3 for the May–June effusive activity at the SEC (De Beni et al., 2021); no estimations are available for the weak 2019–20 effusive/explosive activity at Voragine]. If one looks at the two paroxysmal sequences before and after the 2015–16 Voragine episodes, it becomes clear how magma volumes during 2011–2013 were on the same order of magnitude of those erupted on 2020–2022. However, the former ones were erupted over three years of eruptions, whereas the latter barely in one year (80×10^6 m^3 vs. 108×10^6 m^3).

The possibility to move upward volatile-rich, undegassed magmas suggests that the plumbing system is currently able to drain in an efficient manner most of the magma injected into its deepest levels. The eruptive activity at the surface is then strictly correlated with the magma volume injected and also depends on its ability to degas during the ascent, in a way that the slower the ascent the more efficient is the degassing process (Zuccarello et al., 2021, 2022). Fast timescales of transfer from the deepest levels of the feeding system of conspicuous volumes of magma are therefore the main cause for the exceptional eruptive frequency and explosivity observed during the 2020–22 paroxysmal sequence and explain the conservation of the most mafic compositions associated to these energetic manifestations. This study opens new perspectives for investigating the explosive basaltic volcanism at the most active open vent volcano worldwide, supporting the idea that, at present, the magma supply of Mt. Etna develops along two main trends: replenishment by deeper/huger volumes of volatile-rich magma leads to faster upward migration and stronger eruptions, while replenishment by deeper/littler volumes of volatile-rich magma leads to slower upward migration and weaker eruptions.

Declaration of Competing Interest

The authors declare that they have no known competing financial interests or personal relationships that could have appeared to influence the work reported in this paper.

Data availability

All the data used in this work are available in tables and the supplementary materials linked to the online version of the article.

Acknowledgements

This work was supported by the funding program PIACERI 2020-22 of the University of Catania, project PAROSSISMA, code 22722132140 (Principal Investigator M. Viccaro). The Authors greatly thank Maira Basile, Marco Borzì, Rosario Calcagno, Giorgio Costa, Luca Frasca, Francesco Furia, Vincenzo Greco, Mirko Messina, Marco Sapienza and Mariabenedetta Scandura who contributed, to a various extent, to lava and tephra sampling during the 2020-22 paroxysmal sequence at Mt. Etna. The Authors are also very grateful to the support received by Giancarlo Niceforo for the XRF analyses at the University of Calabria and by Alfio Viola for the SEM-EDS/WDS in situ measurements at the University of Catania. Authors are really thankful to Arturo Gomez-Tuena for the manuscript handling and to Wendy Bohrson and Martin Mangler for their useful comments that greatly improved the early submitted version of this work.

Appendix

Sampling and analytical procedures

The volcanic samples examined in this work cover the interval of activity at Mt. Etna in the period December 13–14, 2020 - February 21, 2022. Tephra samples include coarse-grained lapilli (10–20 mm in diameter), fine-grained lapilli (2–10 mm in diameter) and ashes, which were all taken at the summit area and/or at different sites on the volcano slopes during or just within a few hours since the end of the lava fountaining episode with consequent fallout. Samples that have been used for the present study refers to the eruptive episodes listed in Table 1. Samples were inspected on polished thin sections under optical and electron microscopy. Microanalytical data on minerals were acquired at the Dipartimento di Scienze Biologiche, Geologiche e Ambientali of the University of Catania using a Tescan Vega-LMU scanning electron microscope (SEM) equipped with an EDAX Neptune XM4–60 microanalyzer operating by energy dispersive system (EDS). The microscope is equipped with an ultra-thin Be window, and it is coupled with an EDAX WDS LEXS (wavelength dispersive low energy Xray spectrometer) calibrated for light elements. Operating conditions were set at 20 kV accelerating voltage and 8 nA beam current to acquire high-contrast back-scattered electron images (BSE; 1024 × 864 pixels) and 20 kV accelerating voltage and 2 nA beam current to obtain major element concentrations of crystals and glasses. Repeated analyses on SPI 02753-AB Serial KF certified standard glass during the analytical runs provided precision for all measured elements of around 3–5%. Major element abundances were measured along core-to-rim traverses for a selection of 250 olivine crystals. Analytical traverses were done parallel to the longest side and crosscutting the center of olivine, with spacing between individual spots of 2–7 μm depending on the crystal size. The composition of plagioclase, clinopyroxene and opaque oxides was obtained by single analytical spots collected at the core and rim of the crystals.

Olivine classification and diffusion chronometry approach

We modeled the diffusive relaxation of n. 71 zoned olivine to derive the timescales of magmatic processes drawn out from the examination of olivine populations and types of zoning. The modeling was performed numerically in one dimension with the method of finite differences (Costa et al., 2008) considering constant boundary conditions. A step-like distribution was applied as initial concentration profile to model both normal and reverse zoning patterns. The choice of step-like initial profile follows the assumption that diffusion started as the crystal is incorporated in a magmatic environment having thermodynamic characteristics different than the initial environment, and that the new conditions were able to produce abrupt compositional changes in the crystal. Consequently, the chemical relaxation of a zoned olivine profile was modeled at the temperature of the final host environment (i.e., isothermal diffusion). Most of the modeled crystals exhibit one simple normal (e.g., Type 2 and Type 3) or reverse zoning (e.g., Type 5 and Type 6) and have been therefore modeled with a single step-function. For crystals with more complex zoning (e.g., Type 4, Type 7 and Type 8), the modeling was performed only for the interior zone because the chemical gradient rimward is recorded by just few analytical spots or it is too small (~1 Fo mol%) to be modeled. In four crystals, the complex zoning was modeled non-isothermally in separate steps, assuming one re-equilibration temperature for the interior zone and one for the rim zone.

We accounted for the effects of diffusion anisotropy in olivine by determining the orientation of the olivine a-, b- and c- crystallographic axes and the angles between the SEM-EDS/WDS traverses and the three axes. The crystallographic axes were measured by conoscopic observations under a polarizing optical microscope equipped with a Zeiss 4 axis universal stage. Data were plotted onto a lower hemisphere stereographic projection to measure the α, β and γ angle between the orientation of axes and the analytical traverse, which were finally used to calculate appropriated Fe-Mg diffusion coefficients ($D_{Fe\text{-}Mg}$; Dohmen and Chakraborty, 2007). A diffusion coefficient was determined for any observed olivine population by adopting the thermodynamic parameters (T, P, and fO_2) that define the physical environment of crystallization of a given olivine, as described in Chapters 4 and 5 of this study.

Among the numerous olivine crystals exposed in the two-dimensional thin sections, we modeled only those crystals fulfilling the robustness criteria for reliable time estimates, in accordance with the conditions stated in many studies (Costa and Chakraborty, 2004; Costa et al., 2008; Shea et al., 2015a, 2015b). Because the largest errors result from modeling profiles in sections that are oblique to crystal faces, we disregard the smallest crystals, which have high probability of being off-center sections of an olivine and often generate apparent concentration gradients of different widths (Wallace and Bergantz, 2003). Moreover, we have selected only sections cutting the crystal close to the fastest diffusion direction (i.e., the c-axis; Costa and Chakraborty, 2004). Concentration profiles obtained from randomly sectioned olivine crystals were neither considered for the diffusion modeling nor for the classification of olivine zoning types. Uncertainties on diffusion timescales were obtained by propagating the error in the determination of diffusion coefficients, following the error propagation procedure described by Kahl et al. (2015). We assumed uncertainties of ±20 °C on temperature and $\pm 1.10 \times 10^{-10}$ bars on fO_2 on the basis of the ranges in temperature and oxygen fugacity calculated thermodynamically for the environments of crystallization (and the associated olivine populations). All timescales are referred to as 'maximum' due to the assumption that the observed zoned profile originated by diffusion only (Costa et al., 2008).

Appendix A. Supplementary data

Supplementary data to this article can be found online at https://doi.org/10.1016/j.earscirev.2023.104563.

References

Allard, P., Jean-Baptiste, P., D'Alessandro, W., Parello, F., Parisi, B., Flehoc, C., 1997. Mantle-derived helium and carbon in groundwaters and gases of Mount Etna,Italy. Earth Planet. Sci. Lett. 148, 501–516. https://doi.org/10.1016/S0012-821X(97)00052-6.

Aloisi, M., Shuanggen, J., Pulvirenti, F., Scaltrito, A., 2017. The December 2015 Mount Etna eruption: an analysis of inflation/deflation phases and faulting processes. J. Geodynam. 107, 34–45. https://doi.org/10.1016/j.jog.2017.03.003.

Andronico, D., Branca, S., Calvari, S., Burton, M., Caltabiano, T., Corsaro, R.A., Del Carlo, P., Garfi, G., Lodato, L., Miraglia, L., Murè, F., Neri, M., Pecora, E., Pompilio, M., Salerno, G., Spampinato, L., 2005. A multi-disciplinary study of the 2002–03 Etna eruption: Insights into a complex plumbing system. Bull. Volcanol. 67, 314–330. https://doi.org/10.1007/s00445-004-0372-8.

Andronico, D., Cristaldi, A., Scollo, S., 2008. The 4–5 September 2007 lava fountain at South-East Crater of Mt Etna.Italy. J. Volcanol. Geotherm. Res. 173, 325–328. https://doi.org/10.1016/j.jvolgeores.2008.02.004.

Andronico, D., Corsaro, R.A., 2011. Lava fountains during the episodic eruption of South-East Crater (Mt. Etna), 2000: Insights into magma-gas dynamics within the shallow volcano plumbing system. Bull. Volcanol. 73, 1165–1178. https://doi.org/10.1007/s00445-011-0467-y.

Armienti, P., Barberi, F., Innocenti, F., Pompilio, M., Romano, R., Villari, L., 1984. Compositional variation in the 1983 and other recent Etnean lavas: Insights on the shallow feeding system. Bull. Volcanol. 47, 995–1007. https://doi.org/10.1007/BF01952357.

Armienti, P., Clocchiatti, R., D'Orazio, M., Innocenti, F., Petrini, R., Pompilio, M., Tonarini, S., Villari, L., 1994. The long-standing 1991–1993 Mt. Etna eruption: Petrography and Geochemistry of lavas. Acta Vulcanol. 4, 15–28.

Armienti, P., D'Orazio, M., Innocenti, F., Tonarini, S., Villari, L., 1996. October 1995-February 1996 Mt. Etna explosive activity: Trace element and isotopic constraints on the feeding system. Acta Vulcanol. 8, 1, 1–6.

Asimow, P.D., Ghiorso, M.S., 1998. Algorithmic modifications extending MELTS to calculate subsolidus phase relations. Am. Mineral. 83, 1127–1132. https://doi.org/10.2138/am-1998-9-1022.

Behncke, B., Branca, S., Corsaro, R.A., De Beni, E., Miraglia, L., Proietti, C., 2014. The 2011–2012 summit activity of Mount Etna: birth, growth and products of the new SE crater. J. Volcanol. Geotherm. Res. 270, 10–21. https://doi.org/10.1016/j.jvolgeores.2013.11.012.

Bisson, M., Spinetti, C., Andronico, D., Palaseanu-Lovejoy, M., Buongiorno, F.M., Alexandrov, O., Cecere, T., 2021. Ten years of volcanic activity at Mt Etna: High-

resolution mapping and accurate quantification of the morphological changes by Pleiades and Lidar data. Int. J. Appl. Earth. Obs. Geoinf. 102, 102369 https://doi.org/10.1016/j.jag.2021.102369.
Bonaccorso, A., D'Amico, S., Mattia, M., Patanè, D., 2004. Intrusive mechanisms at Mt. Etna forerunning the July-August 2001 eruption from seismic and ground deformation data. Pure Appl. Geophys. 161, 1469–1487. https://doi.org/10.1007/s00024-004-2515-4.
Bonaccorso, A., Bonforte, A., Calvari, S., Del Negro, C., Di Grazia, G., Ganci, G., Neri, M., Vicari, A., Boschi, E., 2011. The initial phases of the 2008–2009 Mount Etna eruption: a multidisciplinary approach for hazard assessment. J. Geophys. Res. Solid Earth 116, B03203. https://doi.org/10.1029/2010JB007906.
Bonaccorso, A., Calvari, S., 2013. Major effusive eruptions and recent lava fountains: Balance between expected and erupted magma volumes at Etna volcano. Geophys. Res. Lett. 40, 6069–6073. https://doi.org/10.1002/2013GL058291.
Bonaccorso, A., Calvari, S., 2017. A new approach to investigate an eruptive paroxysmal sequence using camera and strainmeter networks: Lessons from the 3–5 December 2015 activity at Etna volcano. Earth Planet. Sci. Lett. 475, 231–241. https://doi.org/10.1016/j.epsl.2017.07.020.
Bonforte, A., Fanizza, G., Greco, F., Matera, A., Sulpizio, R., 2017. Long-term dynamics across a volcanic rift: 21years of microgravity and GPS observations on the southern flank of Mt. Etna volcano. J. Volcanol. Geotherm. Res. 344, 174–184.
Borzì, A.M., Giuffrida, M., Zuccarello, F., Palano, M., Viccaro, M., 2020. The Christmas 2018 eruption at Mount Etna: enlightening how the volcano factory works through a multiparametric inspection. Geochem. Geophys. Geosyst. 21 https://doi.org/10.1029/2020GC009226 e2020GC009226.
Branca, S., Del Carlo, P., 2004. Eruptions of Mt. Etna during the past 3200 years: a revised compilation integrating the historical and stratigraphic records, in Mt. Etna: Volcano Laboratory. In: Bonaccorso, A. (Ed.), Geophys. Monogr, vol. 143. AGU, Washington, DC, pp. 1–27.
Branca, S., Coltelli, M., De Beni, E., Wijbrans, J., 2008. Geological evolution of Mount Etna volcano (Italy) from earliest products until the first central volcanism (between 500 and 100 ka ago) inferred from geochronological and stratigraphic data. Int. J. Earth Sci. 97, 135–152. https://doi.org/10.1007/s00531-006-0152-0.
Bruno, V., Aloisi, M., Gambino, S., Mattia, M., Ferlito, C., Rossi, M., 2022. The most intense deflation of the last two decades at Mt. Etna: The 2019–2021 evolution of ground deformation and modeled pressure sources. Geophys. Res. Lett. 49 https://doi.org/10.1029/2021GL095195 e2021GL095195.
Calvari, S., Bilotta, G., Bonaccorso, A., Caltabiano, T., Cappello, A., Corradino, C., Del Negro, C., Ganci, G., Neri, M., Pecora, E., Salerno, G.G., Spampinato, L., 2020. The VEI 2 Christmas 2018 Etna eruption: a small but intense eruptive event or the starting phase of a larger one? Rem. Sens. 12 (6), 905. https://doi.org/10.3390/rs12060905.
Calvari, S., Biale, E., Bonaccorso, A., Cannata, A., Carleo, L., Currenti, G., Di Grazia, G., Ganci, G., Iozzia, A., Pecora, E., Prestifilippo, M., Sciotto, M., Scollo, S., 2022. Explosive paroxysmal events at Etna Volcano of different magnitude and intensity explored through a multidisciplinary monitoring system. Rem. Sens. 14, 4006. https://doi.org/10.3390/rs14164006.
Calvari, S., Nunnari, G., 2022. Comparison between automated and manual detection of lava fountains from fixed monitoring thermal cameras at Etna Volcano,Italy. Rem. Sens. 14 (10), 2392. https://doi.org/10.3390/rs14102392.
Cannata, A., Spedalieri, G., Behncke, B., Cannavò, F., Di Grazia, G., Gambino, S., Gresta, S., Gurrieri, S., Liuzzo, M., Palano, M., 2015. Pressurization and depressurization phases inside the plumbing system of Mount Etna volcano: evidence from a multiparametric approach. J. Geophys. Res. Solid Earth 120, 5965–5982. https://doi.org/10.1002/2015JB012227.
Cannata, A., Di Grazia, G., Giuffrida, M., Gresta, S., Palano, M., Sciotto, M., Viccaro, M., Zuccarello, F., 2018. Space-time evolution of magma storage and transfer at Mt. Etna volcano (Italy): the 2015–2016 reawakening of Voragine crater. Geochem. Geophys. Geosyst. 19, 471–495. https://doi.org/10.1002/2017GC007296.
Cappello, A., Ganci, G., Bilotta, G., Herault, A., Zago, V., Del Negro, C., 2019. Satellite-driven modeling approach for monitoring lava flow hazards during the 2017 Etna eruption. Ann. Geophys. 62, 2. https://doi.org/10.4401/ag-7792.
Clocchiatti, R., Condomines, M., Guénot, N., Tanguy, J.C., 2004. Magma changes at Mount Etna: the 2001 and 2002–2003 eruptions. Earth Planet. Sci. Lett. 226, 397–414. https://doi.org/10.1016/j.epsl.2004.07.039.
Collins, S.J., Pyle, D.M., Maclennan, J., 2009. Melt inclusions track pre-eruption storage and dehydration of magmas at Etna. Geology 37, 571–574. https://doi.org/10.1130/G30040A.1.
Condomines, M., Tanguy, J.C., Michaud, V., 1995. Magma dynamics at Mt Etna: Constraints from U-Th-Ra-Pb radioactive disequilibria and Sr isotopes in historical lavas. Earth Planet. Sci. Lett. 132, 25–41. https://doi.org/10.1016/0012-821X(95)00052-E.
Corsaro, R.A., Miraglia, L., 2014. The transition from summit to flank activity at Mt. Etna, Sicily (Italy): Inferences from the petrology of products erupted in 2007–2009. J. Volcanol. Geotherm. Res. 275, 51–60. https://doi.org/10.1016/j.jvolgeores.2014.02.009.
Corsaro, R.A., Miraglia, L., 2022. Near real-time petrologic monitoring on volcanic glass to infer magmatic processes during the February-April 2021 paroxysms of the South-East Crater,Etna. Front. Earth. Sci. 10, 828026 https://doi.org/10.3389/feart.2022.828026.
Corsaro, R.A., Pompilio, M., 2004. Buoyancy-controlled eruptions of magmas at Mt.Etna. Terra Nova 16, 6–22. https://doi.org/10.1046/j.1365-3121.2003.00520.x.
Corsaro, R.A., Andronico, D., Behncke, B., Branca, S., Caltabiano, T., Ciancitto, F., Cristaldi, A., De Beni, E., La Spina, A., Lodato, L., Miraglia, L., 2017. Monitoring the December 2015 summit eruptions of Mt. Etna (Italy): Implications on eruptive dynamics. J. Volcanol. Geotherm. Res. 341, 53–69. https://doi.org/10.1016/j.jvolgeores.2017.04.018.
Costa, F., Chakraborty, S., 2004. Decadal time gaps between mafic intrusion and silicic eruption obtained from chemical zoning patterns in olivine. Earth Planet. Sci. Lett. 227, 517–530. https://doi.org/10.1016/j.epsl.2004.08.011.
Costa, F., Dohmen, R., Chakraborty, S., 2008. Time scales of magmatic processes from modeling the zoning patterns of crystals. Rev. Mineral. Geochem. 69, 545–594. https://doi.org/10.2138/rmg.2008.69.14.
Costa, G., Mereu, L., Prestifilippo, M., Scollo, S., Viccaro, M., 2023. Modeling the trajectories of ballistics in the summit area of Mt. Etna (Italy) during the 2020–2022 sequence of lava fountains. Geosciences 13 (5), 145. https://doi.org/10.3390/geosciences13050145.
Currenti, G., Bonaccorso, A., 2019. Cyclic magma recharge pulses detected by high-precision strainmeter data: the case of 2017 inter-eruptive activity at Etna volcano. Sci. Rep. 9 https://doi.org/10.1038/s41598-019-44066-w.
De Beni, E., Behncke, B., Branca, S., Nicolosi, I., Carluccio, R., Caracciolo, F.A., Chiappini, M., 2015. The continuing story of Etna's New Southeast Crater (2012–2014): Evolution and volume calculations based on field surveys and aerophotogrammetry. J. Volcanol. Geotherm. Res. 303, 175–186. https://doi.org/10.1016/j.jvolgeores.2015.07.021.
De Beni, E., Cantarero, M., Messina, A., 2019. UAVs for volcano monitoring: a new approach applied on an active lava flow on Mt. Etna (Italy), during the 27 February–02 March 2017 eruption. J. Volcanol. Geotherm. Res. 369, 250–262. https://doi.org/10.1016/j.jvolgeores.2018.12.001.
De Beni, E., Cantarero, M., Neri, M., Messina, A., 2021. Lava flows of Mt Etna, Italy: the 2019 eruption within the context of the last two decades (1999–2019). J. Maps 17, 65–76. https://doi.org/10.1080/17445647.2020.1854131.
De Gori, P., Giampiccolo, E., Cocina, O., Branca, S., Doglioni, C., Chiarabba, C., 2021. Re-pressurized magma at Mt. Etna, Italy, may feed eruptions for years. Commun. Earth Environ. 2, 216. https://doi.org/10.1038/s43247-021-00282-9.
Di Grazia, G., Cannata, A., Montalto, P., Patanè, D., Privitera, E., Zuccarello, L., Boschi, E., 2009. A multiparameter approach to volcano monitoring based on 4D analyses of seismo-volcanic and acoustic signals: The 2008 Mt. Etna eruption. Geophys. Res. Lett. 36, L18307. https://doi.org/10.1029/2009GL039567.
Dohmen, R., Chakraborty, S., 2007. Fe–Mg diffusion in olivine II: point defect chemistry, change of diffusion mechanisms and a model for calculation of diffusion coefficients in natural olivine. Phys. Chem. Miner. 34, 409–430. https://doi.org/10.1007/s00269-007-0158-6.
Edwards, M.J., Pioli, L., Andronico, D., Scollo, S., Ferrari, F., Cristaldi, A., 2018. Shallow factors controlling the explosivity of basaltic magmas: the 17–25 May 2016 eruption of Etna Volcano (Italy). J. Volcanol. Geotherm. Res. 357, 425–436. https://doi.org/10.1016/j.jvolgeores.2018.05.015.
Edwards, M.J., Eychenne, J., Pioli, L., 2021. Formation and dispersal of ash at open conduit basaltic volcanoes: Lessons from Etna. Front. Earth Sci. 9, 709657 https://doi.org/10.3389/feart.2021.709657.
Fornaciai, A., Andronico, D., Favalli, M., Spampinato, L., Branca, S., Lodato, L., Bonforte, A., Nannipieri, L., 2021. The 2004–2005 Mt. Etna compound lava flow field: a retrospective analysis by combining remote and field methods. J. Geophys. Res. Solid Earth 126. https://doi.org/10.1029/2020JB020499 e2020JB02049.
Ganci, G., Bilotta, G., Zuccarello, F., Calvari, S., Cappello, A., 2023. A multi-sensor satellite approach to characterize the volcanic deposits emitted during Etna's lava fountaining: the 2020–2022 study case. Rem. Sens. 15, 916. https://doi.org/10.3390/rs15040916.
Ganci, G., Cappello, A., Bilotta, G., Herault, A., Zago, V., Del Negro, C., 2018. Mapping volcanic deposits of the 2011–2015 Etna eruptive events using satellite Remote Sensing. Front. Earth Sci. 6, 83. https://doi.org/10.3389/feart.2018.00083.
Ganci, G., Cappello, A., Zago, V., Bilotta, G., Hérault, A., Del Negro, C., 2019. 3D lava flow mapping of the 17–25 May 2016 Etna eruption using tri-stereo optical satellite data. Ann. Geophys. 62 (2), VO220. https://doi.org/10.4401/ag-7875.
Ghiorso, M.S., Sack, R.O., 1995. Chemical mass transfer in magmatic processes IV. A revised and internally consistent thermodynamic model for the interpolation and extrapolation of liquid-solid equilibria in magmatic systems at elevated temperatures and pressures. Contrib. Mineral. Petrol. 119, 197–212. https://doi.org/10.1007/BF00307281.
Ghiorso, M.S., Gualda, G.A.R., 2015. An H2O–CO2 mixed fluid saturation model compatible with rhyolite-MELTS. Contrib. Mineral. Petrol. 169, 53. https://doi.org/10.1007/s00410-015-1141-8.
Giacomoni, P.P., Coltorti, M., Mollo, S., Ferlito, C., Braiato, M., Scarlato, P., 2018. The 2011–2012 paroxysmal eruptions at Mt. Etna volcano: Insights on the vertically zoned plumbing system. J. Volcanol. Geotherm. Res. 349, 370–391. https://doi.org/10.1016/j.jvolgeores.2017.11.023.
Gillot, P.Y., Lefèvre, J.C., Nativel, P.E., 1994. Model for the structural evolution of the volcanoes of Réunion Island. Earth Planet. Sci. Lett. 122, 291–302. https://doi.org/10.1016/0012-821X(94)90003-5.
Giuffrida, M., Viccaro, M., 2017. Three years (2011–2013) of eruptive activity at Mt. Etna: working modes and timescales of the modern volcano plumbing system from micro-analytical studies of crystals. Earth-Sci. Rev. 171, 289–322. https://doi.org/10.1016/j.earscirev.2017.06.003.
Giuffrida, M., Holtz, F., Vetere, F., Viccaro, M., 2017. Effects of CO2 flushing on crystal textures and compositions: experimental evidence from recent K-trachybasalts erupted at Mt.Etna. Contrib. Mineral. Petrol. 172, 90. https://doi.org/10.1007/s00410-017-1408-3.
Giuffrida, M., Viccaro, M., Ottolini, L., 2018. Ultrafast syn-eruptive degassing and ascent trigger high-energy basic eruptions. Sci. Rep. 8, 147. https://doi.org/10.1038/s41598-017-18580-8.

Giuffrida, M., Scandura, M., Costa, G., Zuccarello, F., Sciotto, M., Cannata, A., Viccaro, M., 2021. Tracking the summit activity of Mt. Etna volcano between July 2019 and January 2020 by integrating petrological and geophysical data. J. Volcanol. Geotherm. Res. 418, 107350. https://doi.org/10.1016/j.jvolgeores.2021.107350.

Gualda, G.A.R., Ghiorso, M.S., Lemons, R.V., Carley, T.L., 2012. Rhyolite-MELTS: a modified calibration of MELTS optimized for silica-rich, fluid-bearing magmatic systems. J. Petrol. 53, 875–890. https://doi.org/10.1093/petrology/egr080.

Harris, A., Steffke, A., Calvari, S., Spampinato, L., 2011. Thirty years of satellite-derived lava discharge rates at Etna: Implications for steady volumetric output. J. Geophys. Res. Solid Earth 116, B08204. https://doi.org/10.1029/2011JB008237.

Kahl, M., Chakraborty, S., Costa, F., Pompilio, M., 2011. Dynamic plumbing system beneath volcanoes revealed by kinetic modeling, and the connection to monitoring data: An example from Mt. Etna. Earth Planet. Sci. Lett. 308, 11–22. https://doi.org/10.1016/j.epsl.2011.05.008.

Kahl, M., Chakraborty, S., Costa, F., Pompilio, M., Liuzzo, M., Viccaro, M., 2013. Compositionally zoned crystals and real-time degassing data reveal changes in magma transfer dynamics during the 2006 summit eruptive episodes of Mt.Etna. Bull. Volcanol. 75, 692. https://doi.org/10.1007/s00445-013-0692-7.

Kahl, M., Chakraborty, S., Pompilio, M., Costa, F., 2015. Constraints on the nature and evolution of the magma plumbing system of Mt. Etna volcano (1991–2008) from a combined thermodynamic and kinetic modelling of the compositional record of minerals. J. Petrol. 56, 2025–2068. https://doi.org/10.1093/petrology/egv063.

Kahl, M., Viccaro, M., Ubide, T., Morgan, D.J., Dingwell, D.B., 2017. A branched magma feeder system during the 1669 eruption of Mt Etna: evidence from a time-integrated study of zoned olivine phenocryst populations. J. Petrol. 58, 443–472. https://doi.org/10.1093/petrology/egx022.

La Delfa, S., Patanè, G., Clocchiatti, R., Joron, J.L., Tanguy, J.C., 2001. Activity of Mount Etna preceding the February 1999 fissure eruption: inferred mechanism from seismological and geochemical data. J. Volcanol. Geotherm. Res. 105, 121–139. https://doi.org/10.1016/S0377-0273(00)00249-3.

Lanzafame, G., Ferlito, C., Donato, S., 2018. Combining chemical and X-ray microtomography investigations on crustal xenoliths at Mount Etna: evidence of volcanic gas fluxing. Ann. Geophys. 61 https://doi.org/10.4401/ag-7740.

Lentini, F., 1982. The geology of the Mt Etna basement. Memorie della Società Geologica Italiana 23, 7–25.

Magee, R., Ubide, T., Kahl, M., 2020. The lead-up to Mount Etna's most destructive historic eruption (1669). Cryptic recharge recorded in clinopyroxene. J. Petrol 61 (1). https://doi.org/10.1093/petrology/egaa025 egaa025.

Métrich, N., Allard, P., Spilliaert, N., Andronico, D., Burton, M., 2004. 2001 flank eruption of the alkali- and volatile-rich primitive basalt responsible for Mount Etna's evolution in the last three decades. Earth Planet. Sci. Lett. 228, 1–17. https://doi.org/10.1016/j.epsl.2004.09.036.

Miraglia, L., 2021. Etna glass analyses 2013 (GMCET_2013) (Version 1) [Data set]. Istituto Nazionale di Geofisica e Vulcanologia (INGV). https://doi.org/10.13127/etna/gmc_2013.

Mollo, S., Giacomoni, P.P., Coltorti, M., Ferlito, C., Iezzi, G., Scarlato, P., 2015. Reconstruction of magmatic variables governing recent Etnean eruptions: constraints from mineral chemistry and P-T-fO2-H2O modelling. Lithos 212–215, 311–320. https://doi.org/10.1016/j.lithos.2014.11.020.

Mollo, S., Pontesilli, A., Moschini, P., Palummo, F., Taddeucci, J., Andronico, D., Del Bello, E., Scarlato, P., 2022. Modeling the crystallization conditions of clinopyroxene crystals erupted during February–April 2021 lava fountains at Mt. Etna: Implications for the dynamic transfer of magmas. Lithos 420–421, 106710. https://doi.org/10.1016/j.lithos.2022.106710.

Nicotra, E., Viccaro, M., 2012a. Unusual magma storage conditions at Mt. Etna (Southern Italy) as evidenced by plagioclase megacryst-bearing lavas: implications for the plumbing system geometry and summit caldera collapse. Bull. Volcanol. 74, 795–815. https://doi.org/10.1007/s00445-011-0566-9.

Nicotra, E., Viccaro, M., 2012b. Transient uprise of gas and gas-rich magma batches fed the pulsating behaviour of the 2006 eruptive episodes at Mt. Etna volcano. J. Volcanol. Geotherm. Res. 227–228, 102–118. https://doi.org/10.1016/j.jvolgeores.2012.03.004.

Paonita, A., Liuzzo, M., Salerno, G., Federico, C., Bonfanti, P., Caracausi, A., Giuffrida, G., La Spina, A., Caltabiano, T., Gurrieri, S., Giudice, G., 2021. Intense overpressurization at basaltic open-conduit volcanoes as inferred by geochemical signals: The case of the Mt. Etna December 2018 eruption. Sci. Adv. 7 (36) https://doi.org/10.1126/sciadv.abg6297 eabg6297.

Patanè, D., Aiuppa, A., Aloisi, M., Behncke, B., Cannata, A., Coltelli, M., Di Grazia, G., Gambino, S., Gurrieri, S., Mattia, M., Salerno, G., 2013. Insights into magma and fluid transfer at Mount Etna by a multiparametric approach: A model of the events leading to the 2011 eruptive cycle. J. Geophys. Res. Solid Earth 118, 3519–3539. https://doi.org/10.1002/jgrb.50248.

Pompilio, M., Bertagnini, A., Del Carlo, P., Di Roberto, A., 2017. Magma dynamics within a basaltic conduit revealed by textural and compositional features of erupted ash: the December 2015 Mt.Etna paroxysms. Sci. Rep. 7, 4805. https://doi.org/10.1038/s41598-017-05065-x.

Shea, T., Costa, F., Krimer, D., Hammer, J.E., 2015a. Accuracy of timescales retrieved from diffusion modeling in olivine: a 3D perspective. Am. Mineral. 100, 2026–2042. https://doi.org/10.2138/am-2015-5163.

Shea, T., Lynn, K.J., Garcia, M.O., 2015b. Cracking the olivine zoning code: Distinguishing between crystal growth and diffusion. Geology 43, 935–938. https://doi.org/10.1130/G37082.1.

Spilliaert, N., Allard, P., Métrich, N., Sobolev, A.V., 2006. Melt inclusion record of the conditions of ascent, degassing, and extrusion of volatile-rich alkali basalt during the powerful 2002 flank eruption of Mount Etna (Italy). J. Geophys. Res. Solid Earth 111, B4. https://doi.org/10.1029/2005JB003934.

Tanguy, J.C., 1978. Tholeiitic basalt magmatism of Mount Etna and its relations with the alkaline series. Contrib. Mineral. Petrol. 66, 51–67. https://doi.org/10.1007/BF00376085.

Tanguy, J.C., Clocchiatti, R., 1984. The Etnean lavas, 1977–1983: petrology and mineralogy. Bull. Volcanol. 47, 879–894. https://doi.org/10.1007/BF01952349.

Tanguy, J.C., Condomines, M., Kieffer, G., 1997. Evolution of the Mount Etna magma: Constraints on the present feeding system and eruptive mechanism. J. Volcanol. Geotherm. Res. 75, 221–250. https://doi.org/10.1016/S0377-0273(96)00065-0.

Tonarini, S., Armienti, P., D'Orazio, M., Innocenti, F., Pompilio, M., Petrini, R., 1995. Geochemical and isotopic monitoring of Mt. Etna 1989–1993 eruptive activity: bearing on the shallow feeding system. J. Volcanol. Geotherm. Res. 64, 95–115. https://doi.org/10.1016/0377-0273(94)00039-J.

Ubide, T., Kamber, B.S., 2018. Volcanic crystals as time capsules of eruption history. Nat. Comm. 9 (1), 326. https://doi.org/10.1038/s41467-017-02274-w.

Viccaro, M., Cristofolini, R., 2008. Nature of mantle heterogeneity and its role in the short-term geochemical and volcanological evolution of Mt. Etna (Italy). Lithos 105, 272–288. https://doi.org/10.1016/j.lithos.2008.05.001.

Viccaro, M., Zuccarello, F., 2017. Mantle ingredients for making the fingerprint of Etna alkaline magmas: implications for shallow partial melting within the complex geodynamic framework of Eastern Sicily. J. Geodyn. 109, 10–23. https://doi.org/10.1016/j.jog.2017.06.002.

Viccaro, M., Giacomoni, P.P., Ferlito, C., Cristofolini, R., 2010. Dynamics of magma supply at Mt. Etna volcano (Southern Italy) as revealed by textural and compositional features of plagioclase phenocrysts. Lithos 116, 77–91. https://doi.org/10.1016/j.lithos.2009.12.012.

Viccaro, M., Nicotra, E., Millar, I.L., Cristofolini, R., 2011. The magma source at Mount Etna volcano: Perspectives from the Hf isotope composition of historic and recent lavas. Chem. Geol. 281, 343–351. https://doi.org/10.1016/j.chemgeo.2010.12.020.

Viccaro, M., Garozzo, I., Cannata, A., Di Grazia, G., Gresta, S., 2014. Gas burst vs. Gas-rich magma recharge: a multidisciplinary study to reveal factors controlling triggering of the recent paroxysmal eruptions at Mt.Etna. J. Volcanol. Geotherm. Res. 278–279, 1–13. https://doi.org/10.1016/j.jvolgeores.2014.04.001.

Viccaro, M., Calcagno, R., Garozzo, I., Giuffrida, M., Nicotra, E., 2015. Continuous magma recharge at Mt. Etna during the 2011–2013 period controls the style of volcanic activity and compositions of erupted lavas. Mineral. Petrol. 109, 67–83. https://doi.org/10.1007/s00710-014-0352-4.

Viccaro, M., Barca, D., Bohrson, W.A., D'Oriano, C., Giuffrida, M., Nicotra, E., Pitcher, B. W., 2016a. Crystal residence times from trace element zoning in plagioclase reveal changes in magma transfer dynamics at Mt. Etna during the last 400 years. Lithos 248–251, 309–323. https://doi.org/10.1016/j.lithos.2016.02.004.

Viccaro, M., Zuccarello, F., Cannata, A., Palano, M., Gresta, S., 2016b. How a complex basaltic volcanic system works: Constraints from integrating seismic, geodetic, and petrological data at Mount Etna volcano during the July–August 2014 eruption. J. Geophys. Res. Solid Earth 121, 5659–5678. https://doi.org/10.1002/2016JB013164.

Viccaro, M., Giuffrida, M., Zuccarello, F., Scandura, M., Palano, M., Gresta, S., 2019. Violent paroxysmal activity drives self-feeding magma replenishment at Mt.Etna. Sci. Rep. 9 https://doi.org/10.1038/s41598-019-43211-9.

Wallace, G.S., Bergantz, G.W., 2003. Constraints on mingling of crystal populations from off-center zoning profiles: a statistical approach. Am. Mineral. 89, 64–73.

Zuccarello, F., Schiavi, F., Viccaro, M., 2021. Magma dehydration controls the energy of recent eruptions at Mt.Etna volcano. Terra Nova 33, 423–429. https://doi.org/10.1111/ter.12527.

Zuccarello, F., Schiavi, F., Viccaro, M., 2022. The eruption run-up at Mt. Etna volcano: constraining magma decompression rates and their relationships with the final eruptive energy. Earth Planet. Sci. Lett. 597, 117821 https://doi.org/10.1016/j.epsl.2022.117821.